



**HAL**  
open science

## Calibrating an evapotranspiration model using radiometric surface temperature, vegetation cover fraction and near-surface soil moisture data

Bouchra Ait Hssaine, Olivier Merlin, Zoubair Rafi, Jamal Ezzahar, Lionel Jarlan, Saïd Khabba, Salah Er-Raki

### ► To cite this version:

Bouchra Ait Hssaine, Olivier Merlin, Zoubair Rafi, Jamal Ezzahar, Lionel Jarlan, et al.. Calibrating an evapotranspiration model using radiometric surface temperature, vegetation cover fraction and near-surface soil moisture data. *Agricultural and Forest Meteorology*, 2018, 256-257, pp.104-115. 10.1016/j.agrformet.2018.02.033 . hal-01924705

**HAL Id: hal-01924705**

**<https://hal.science/hal-01924705>**

Submitted on 16 Nov 2018

**HAL** is a multi-disciplinary open access archive for the deposit and dissemination of scientific research documents, whether they are published or not. The documents may come from teaching and research institutions in France or abroad, or from public or private research centers.

L'archive ouverte pluridisciplinaire **HAL**, est destinée au dépôt et à la diffusion de documents scientifiques de niveau recherche, publiés ou non, émanant des établissements d'enseignement et de recherche français ou étrangers, des laboratoires publics ou privés.

# 1 Calibrating an evapotranspiration model using radiometric surface temperature, 2 vegetation cover fraction and near-surface soil moisture data 3

4 Bouchra Ait Hssaine<sup>1,2</sup>, Olivier Merlin<sup>1,2</sup>, Zoubair Rafi<sup>1</sup>, Jamal Ezzahar<sup>3</sup>, Lionel  
5 Jarlan<sup>1,2</sup>, Saïd Khabba<sup>1</sup>, Salah Er-Raki<sup>1</sup>

6 <sup>1</sup>Université Cadi Ayyad, Marrakech, Morocco

7 <sup>2</sup>CESBIO, Université de Toulouse, IRD/CNRS/UPS/CNES, Toulouse, France

8 <sup>3</sup>Equipe de Mathématiques et traitement de l'information (MTI), Ecole Nationale des  
9 Sciences Appliquées, Université Cadi Ayyad, Safi, Morocco

10 Corresponding author: Bouchra Ait Hssaine ([bouchraaitssaine@gmail.com](mailto:bouchraaitssaine@gmail.com))

## 11 Key Points:

- 12
- 13 • TSEB model is enhanced to TSEB-SM model by using surface biophysical  
14 characteristics
  - 15 • Calibration method is developed to retrieve parameters affecting evapotranspiration
  - 16 • The performance of TSEB and TSEB-SM models is evaluated over irrigated wheat  
17 fields
  - 18 • The Priestley-Taylor coefficient is found to vary in time as a function of soil moisture  
19
- 20
- 21

## 22 Abstract

23 An accurate representation of the partitioning between soil evaporation and plant transpiration  
24 is an asset for modeling crop evapotranspiration (ET) along the agricultural season. The Two-  
25 Surface energy Balance (TSEB) model operates the ET partitioning by using the land surface  
26 temperature (LST), vegetation cover fraction ( $f_c$ ), and the Priestley Taylor (PT) assumption  
27 that relates transpiration to net radiation via a fixed PT coefficient ( $\alpha_{PT}$ ). To help constrain the  
28 evaporation/transpiration partition of TSEB, a new model (named TSEB-SM) is developed by  
29 using, in addition to LST and  $f_c$  data, the near-surface soil moisture (SM) as an extra constraint  
30 on soil evaporation. An innovative calibration procedure is proposed to retrieve three key  
31 parameters:  $\alpha_{PT}$  and the parameters ( $a_{RSS}$  and  $b_{RSS}$ ) of a soil resistance formulation. Specifically,  
32  $a_{RSS}$  and  $b_{RSS}$  are retrieved at the seasonal time scale from SM and LST data with  $f_c < 0.5$ , while  
33  $\alpha_{PT}$  is retrieved at the daily time scale from SM and LST data for  $f_c > 0.5$ . The new ET model  
34 named TSEB-SM is tested over 1 flood- and 2 drip-irrigated wheat fields using in situ data  
35 collected during two field experiments in 2002-2003 and 2016-2017. The calibration algorithm  
36 is found to be remarkably stable as  $\alpha_{PT}$ ,  $a_{RSS}$  and  $b_{RSS}$  parameters converge rapidly in few (2-3)  
37 iterations. Retrieved values of  $\alpha_{PT}$ ,  $a_{RSS}$  and  $b_{RSS}$  are in the range 0.0-1.4, 5.7-9.5, and 1.4-6.9,  
38 respectively. Calibrated daily  $\alpha_{PT}$  mainly follows the phenology of winter wheat crop with a  
39 maximum value coincident with the full development of green biomass and a minimum value  
40 reached at harvest. The temporal variations of  $\alpha_{PT}$  before senescence are attributed to the  
41 dynamics of both root-zone soil moisture and the amount of green biomass (vegetation water

42 content). Moreover, the overall (for the three sites) root mean square difference between the  
43 ET simulated by TSEB-SM and eddy-covariance measurements is  $67 \text{ W m}^{-2}$  (24% relative  
44 error), compared to  $108 \text{ W m}^{-2}$  (38% relative error) for the original version of TSEB using  
45 default parameterization ( $\alpha_{\text{PT}} = 1.26$ ). Such a calibration strategy has great potential for  
46 applications at multiple scales using remote sensing data including thermal-derived LST, solar  
47 reflectance-derived  $f_c$  and microwave-derived SM.

## 48 1 Introduction

49 A large variety of evapotranspiration (ET) models and measurements have been reported  
50 in the literature (Allen et al., 2011). However, ET estimation over extended areas including  
51 different biomes and climates is still subject to significant uncertainties (Pereira et al., 2004;  
52 Ershadi et al., 2014). Although the main drivers of ET, such as atmospheric evaporative  
53 demand, vegetation type, development stages and health, surface biophysical characteristics  
54 and soil water availability (e.g. Federer et al., 2003), are now well identified, one major  
55 difficulty in modeling this process lies in a lack of relevant input data available at the desired  
56 space and time scales (Allen et al., 2011; Pereira et al., 2014). The accuracy of ET estimates at  
57 a given scale thus currently represents a trade-off between model complexity and realism,  
58 which is usually related to i) the number of model parameters and forcing variables and ii) the  
59 availability of data that generally decreases with the spatial extent (Allen et al., 2011;  
60 Gharsallah et al., 2014).

61 Regarding data availability over large areas and at multiple scales, remote sensing observations  
62 provide very relevant information to feed ET models such as vegetation indices, land surface  
63 temperature (LST) and near-surface soil moisture (SM). Especially, SM is one of the main  
64 controlling factors of soil evaporation (e.g. Chanzy et al. 1993), vegetation cover fraction ( $f_c$ )  
65 provides an essential structural constraint on evaporation/transpiration partitioning (e.g. Allen  
66 et al. 2000) and LST is a signature of available energy and evapotranspiration (e.g. Norman et  
67 al. 1995). For this reason, efforts have been made to integrate those data as additional and  
68 complementary information on ET (e.g. Price et al., 1990). Through its link with ET under  
69 moisture-limited conditions, LST has been extensively used to retrieve ET at a wide range of  
70 spatial resolutions (Kalma et al., 2008). LST-based ET retrieval methods are generally  
71 classified in two categories. The first one is the so-called “residual” method, which estimates  
72 latent heat flux as a residual term of the surface energy balance (e.g. Norman et al., 1995; Su,  
73 2002). The second one is named the “contextual” method based on the interpretation of the  
74 LST versus vegetation index feature space (e.g. Moran et al., 1994 ; Long and Singh, 2012),  
75 the interpretation of the LST versus albedo feature space (e.g. Roerink et al., 2000), or the  
76 interpretation of both spaces (Merlin 2013; Merlin et al., 2014). The use of SM data, Jung et  
77 al. (2010) related the global ET trend to the SM trend derived from TRMM (Tropical Rainfall  
78 Monitoring Mission) microwave data. At regional scale, ET was found to have a correlation of  
79 about 0.5 with the SM derived from airborne L-band data and a correlation even larger for  $f_c$   
80 values lower than 0.5 (Bindlish et al., 2001; Diarra et al., 2017). This was the basis for  
81 developing ET models based on microwave-derived SM data (Kustas et al., 1998; Bindlish et  
82 al., 2001; Kustas et al., 2003; Li et al., 2006; Gokmen et al., 2012; Li et al., 2015).

83 Among a wide panel of existing ET models, the Priestley Taylor (PT) assumption that  
84 empirically relates ET to net radiation (Priestley and Taylor 1972) has shown a growing interest  
85 (Norman et al., 1995, Kustas and Norman 1999, Li et al., 2005, Anderson et al., 2007, Fisher  
86 et al., 2008, Agam et al., 2010, Jin et al., 2011, Yao et al., 2015, Ai et al., 2016). PT coefficient  
87 noted  $\alpha_{\text{PT}}$  directly relates latent heat flux to the energy available at the surface. Since neglecting  
88 the aerodynamic resistance term included in the full Penman-Monteith equation (Monteith  
89 1965), the PT formulation is relatively simple, requires less input data and has proven to be

90 remarkably accurate and robust for estimating potential ET in a wide range of conditions  
91 (Fisher et al., 2008). It is therefore well suited for operational (McAneney et al., 1996) and  
92 large scale (Anderson et al., 2008) applications. In addition, recent studies based on in situ  
93 global data sets have reported a good robustness of the PT modeling approach over a variety  
94 of biomes (Ershadi et al., 2014). Nevertheless, various theoretical (e.g. De Bruin, 1983) and  
95 experimental (e.g. Fisher et al., 2008) studies have stressed that the PT coefficient is variable  
96 under different surface and atmospheric conditions. In a literature review, the factors that  
97 influence the variability of  $\alpha_{PT}$  are: leaf area index (Fisher et al., 2008; Jin et al., 2011; Ai and  
98 Yang, 2016), the green fraction of canopy (Norman et al., 1995; Fisher et al., 2008), soil water  
99 availability (Davies and Allen, 1973; Mukammal and Neumann 1977; De Bruin, 1983;  
100 Eichinger et al., 1996; Fisher et al., 2008; Jin et al., 2011; Perez et al., 2017; Yao et al., 2017),  
101 vapor pressure deficit or advective conditions (Jury and Tanner, 1975; Kustas et al., 2000;  
102 Agam et al., 2010; Colaizzi et al., 2014), wind speed (Mukammal and Neumann, 1977), air  
103 temperature (Ai and Yang, 2016), air relative humidity (Er-Raki et al., 2010), plant temperature  
104 (Fisher et al., 2008), surface sensible heat flux (Pereira and Nova 1992) and mulch fraction (Ai  
105 and Yang, 2016). As a result of changes in the above ecophysiological and environmental  
106 constraints,  $\alpha_{PT}$  commonly varies in the range 0.5-2.0 with an average value estimated around  
107 1.3 (above references).

108 Data available from space can help in implementing the PT approach from three distinct  
109 perspectives: i) applying a constraint on vegetation transpiration using an a priori value for  $\alpha_{PT}$   
110 (Norman et al., 1995; Kustas et al., 1999; Anderson et al., 2008), ii) applying a constraint on  
111 soil evaporation using SM data (Bindlish et al., 2001; Yao et al., 2017), or iii) retrieving the  
112 PT coefficient from vegetation indices (Fisher et al., 2008; Jin et al., 2011; Yao et al., 2015;  
113 Yao et al., 2017) or from an interpretation of the LST-vegetation index feature space (Jiang  
114 and Islam, 2001; Wang et al., 2006; Perez et al., 2017). While LST, vegetation indices and SM  
115 are alternatively used by satellite-based PT approaches, few studies have combined all three  
116 data types. In fact, most studies have compared LST-based versus SM-based ET models  
117 separately (Kustas et al., 1998; Kustas et al., 2003; Li et al., 2006; Gokmen et al., 2012). Given  
118 that SM controls the soil temperature (via the soil evaporation) and that LST integrates both  
119 soil and vegetation temperatures, the main issue to integrate simultaneously SM and LST into  
120 an unique model is to ensure a robust convergence of soil/vegetation temperatures (Kustas et  
121 al., 2003; Li et al., 2006) and associated evaporation/transpiration fluxes. The recent studies of  
122 Li et al.(2015) and Song et al.(2016) combined LST and SM to better constrain ET but both  
123 approaches relied on a priori reduction coefficients of potential ET. Reduction coefficients of  
124 potential ET are equivalent to the soil evaporative efficiency (defined as the ratio of actual to  
125 potential evaporation, e.g. Merlin et al., 2016) and to the vegetation stress functions (defined  
126 as the ratio of actual to potential transpiration, e.g. Hain et al., 2009) for the soil and vegetation  
127 component, respectively. The point is there is no universal parameterization of both soil  
128 evaporation efficiency and vegetation stress functions. Alternatively, Sun et al. (2012)  
129 proposed an innovative assimilation method to calibrate the parameters of a SVAT (Soil  
130 Vegetation Atmosphere Transfer) model from available remote sensing variables including  
131 LST and SM. Assimilation results improved ET estimates but the retrieved parameters were  
132 mostly conceptual due to the simplicity of the surface model used.

133 In this context, the objective of this paper is: (i) the modification of the PT-based TSEB  
134 formalism (Norman et al., 1995; Kustas et al., 1999) to integrate LST and SM in situ data  
135 simultaneously (the modified version is named TSEB-SM), and (ii) the development of a  
136 calibration procedure of TSEB-SM to retrieve the main parameters of soil evaporation (soil  
137 resistance) and plant transpiration ( $\alpha_{PT}$ ). The approach is tested over three irrigated wheat crops  
138 in the Tensift basin, central Morocco. In each case, the calibration procedure is tested and the

139 TSEB-SM latent and sensible heat fluxes are evaluated and compared against the original  
140 TSEB simulations.

## 141 **2 Methods**

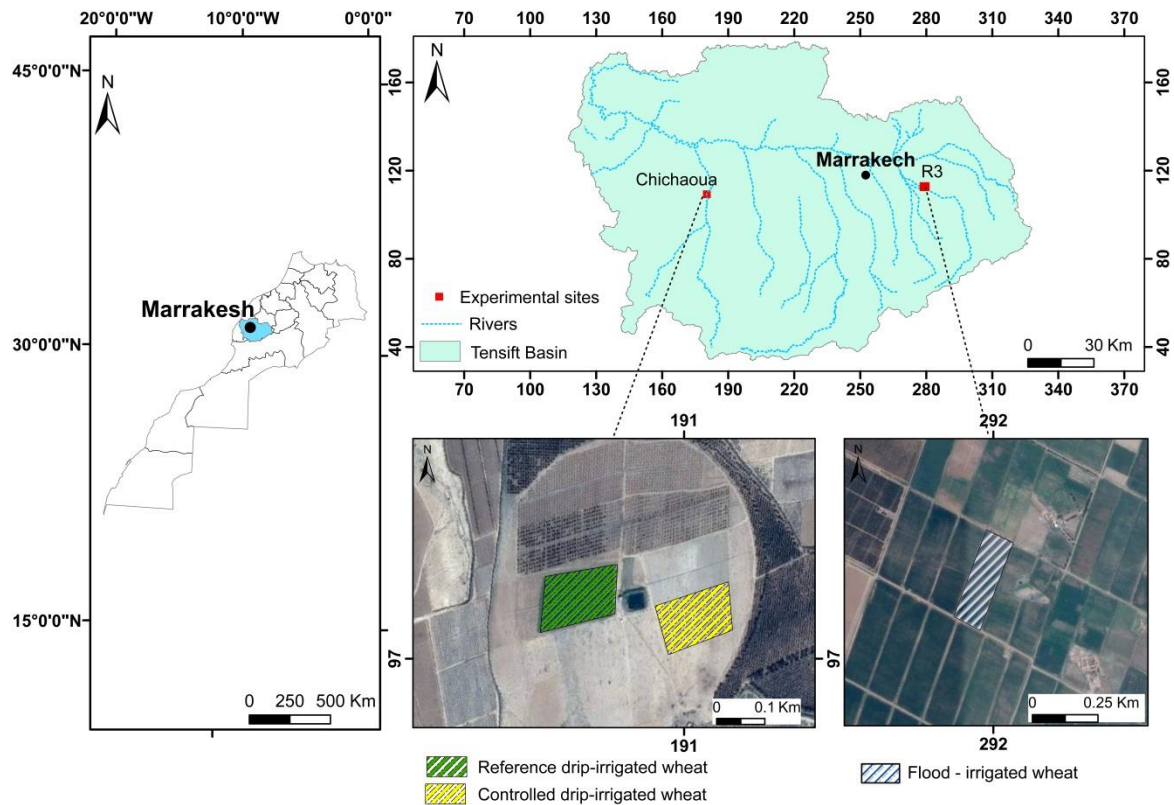
### 142 2.1 Data

#### 143 2.1.1 Sites description

144 The study sites are located in irrigated agricultural areas east (R3 perimeter) and west  
145 (Chichaoua area) of Marrakech city in the Tensift basin, central Morocco (see Figure 1). The  
146 climate in the region is semi-arid, with an average yearly precipitation in the order of 250 mm,  
147 of which approximately 75% falls during the winter and spring (November-April). The average  
148 humidity of the atmosphere is 50% and the reference crop ET is estimated as 1600 mm per year  
149 (Allen et al., 1998), greatly exceeding the annual rainfall.

150 Two data sets are used herein. The first data set was collected from December 2002 to May  
151 2003 over a wheat crop in the R3 zone. The second one was collected from November 2016 to  
152 May 2017 over two wheat crops near Chichaoua. Those experiments were carried out to  
153 monitor the energy and water balance as well as the soil and vegetation characteristics and  
154 conditions during the entire wheat growing cycle. The R3 crop field is 4 ha and is irrigated  
155 through periodic (approximately every 3 weeks) flooding with a mean quantity of 30 mm  
156 regardless of precipitation. Both Chichaoua crop fields are 1.5 ha and are irrigated by drip  
157 technique. During the 2016-17 experiment, one (reference) field was irrigated according to the  
158 crop water needs estimated by the FAO method every 3 to 4 days until mid-April while the  
159 other (controlled) field was irrigated exactly the same way except during controlled stress  
160 periods when irrigation was cut. The mean irrigation quantity was about 15 mm for both crop  
161 fields, whereas the total water supply by drip irrigation was 374 and 504 mm for the controlled  
162 and reference field, respectively.

163



164

165

166

167

Figure 1. Location of the three study sites including a flood-irrigated wheat crop in the R3 zone (east of Marrakech) and two (controlled and reference) drip-irrigated wheat crops near Chichaoua city (west of Marrakech) in the Tensift basin, central Morocco. (Flat area)

168

169

### 170 2.1.2 Surface fluxes

171

172

173

174

175

176

177

178

179

180

181

182

183

184

185

186

187

188

189

An eddy covariance (EC) tower was installed over each field to measure the latent (LE) heat and sensible (H) heat fluxes at a 2-m height. EC systems included a CSAT3 3D sonic anemometer (Campbell scientific Ltd, Logan USA) over the three sites, a LICOR-7500 open-path infrared gas analyzer (Campbell scientific Ltd, Logan USA) installed over the R3 site and a KH20 Krypton hygrometer (Campbell Scientific Ltd, Logan USA) installed over both Chichaoua sites. The half-hourly fluxes were calculated off-line using the EC processing software 'ECpack', after performing all required corrections for planar fit correction, humidity and oxygen (KH20), frequency response for slow apparatus, and path length integration (Van Dijk et al., 2004). EC towers were also equipped with Kipp and Zonen CNR radiometers to measure net radiation ( $R_n$ ) and heat flux plates (Campbell Scientific Ltd, Logan USA) to measure the soil heat flux ( $G$ ). Analysis of the energy balance closure showed that the sum of latent and sensible heat flux measured independently by the EC systems was often lower than the available energy ( $R_n - G$ ). The relative closure was satisfied by about 88%, 64% and 70% (of available energy) for the R3, controlled and reference sites, respectively. This problem could not be explained neither by the mismatch in the spatial extent of flux measurements, nor by the uncertainties associated with the measurements of soil heat flux and net radiation (Twine et al., 2000, Ezzahar et al. 2009, Hoedjes 2008). Correction was hence performed using the approach suggested by Twine et al. (2000). The energy budget closure was forced at the 30 min time step using the daily Bowen ratio (called  $\beta = H/LE$ ). Corrected turbulent fluxes were

190 derived as  $LE = \frac{\beta}{\beta+1} (Rn - G)$  and  $H = \frac{(Rn-G)}{\beta+1}$ , with  $\beta$  computed from the 30-min observed  
 191 H and LE cumulated between 9 am and 5 pm. The Bowen ratio correction enhanced these  
 192 turbulent fluxes by about 21, 39 and 50% for H and 20, 42 and 56% for LE, for R3 zone,  
 193 controlled and reference sites, respectively.

### 194 2.1.3 Land surface temperature, soil moisture and vegetation cover fraction

195 Surface temperature was measured by using an infrared thermometer (IRTS-P) set up at a 2-m  
 196 height above ground. Two sensors, oriented downwards, were used in each field. The measured  
 197 LST is taken as the arithmetical mean of the two independent measurements.

198 Time Domain Reflectometry (TDR) probes (model CS615, CS655) were installed in a soil pit  
 199 near the EC towers to measure soil water content at different soil depths of 5, 10, 20, 30, 50,  
 200 100 cm and 5, 15, 25, 35, 50, 80 cm and 5, 15, 30, 50, 80 cm for the flood-, controlled drip-  
 201 and reference drip-irrigated wheat, respectively. The TDR technique is based on the  
 202 measurement of the soil dielectric constant to estimate its volumetric water content. An  
 203 appropriate calibration of the TDR measurement is necessary because several factors as the  
 204 electrical conductivity, bulk density and soil texture can affect the soil dielectric constant (Topp  
 205 et al., 1980; Regalado et al., 2001; Roth et al., 1992; Tomer et al., 1999; Weitz et al., 1997).  
 206 The field volumetric moisture content was determined using the gravimetric method; three  
 207 samples were collected at installation depth of each TDR probe using a 392.5 cm<sup>3</sup> aluminum  
 208 core. A linear regression was established between the volumetric water content and the square  
 209 root of the TDR time response ( $\tau$  in s) ( $SM = a_{TDR} * \sqrt{\tau} + b_{TDR}$ ).

210 The vegetation cover fraction -defined as the vegetated surface area projected on the ground at  
 211 nadir, per soil surface area unit- was measured routinely within each field using a digital  
 212 photography-based method. Hemispherical photographs were taken at various representative  
 213 points of the field using a Nikon CoolPix camera equipped with a fisheye lens. This method  
 214 binarizes digital photos, in vegetation and soil, based on thresholds in the green and red bands  
 215 (Khabba et al., 2009).  
 216

## 217 2.2 Models and calibration strategies

218 In this section, the main equations of the original version of TSEB model (Norman et al.,  
 219 1995; Kustas et al., 1999) are briefly reproduced and the new TSEB-SM model is fully  
 220 described. Note that the main difference between the two models concerns the treatment of soil  
 221 evaporation, which is either estimated as a residual term for TSEB or explicitly represented  
 222 through a soil resistance term for TSEB-SM.  
 223

### 224 2.2.1 Models

#### 225 A. TSEB model

226 The TSEB model was presented and described by Norman et al., (1995), Norman et al.  
 227 (2000), Kustas and Norman (1999), Timmermans et al (2007), French et al. (2015) and Colaizzi  
 228 et al. (2012). It produces two separate energy balances for the soil and vegetation and estimates  
 229 evaporation and transpiration as residual term of the energy balance. Two variables derived  
 230 from remote sensing instruments are key inputs for TSEB model: The first is the surface  
 231 temperature, which is used to estimate the sensible heat flux and the second is the fraction  
 232 cover, which controls the energy partitioning between surface vegetation and soil.

233 The PT coefficient ( $\alpha_{PT}$ ) is one of the most sensitive parameters of TSEB, because it drives the  
 234 vegetation latent heat flux. Most studies conducted with TSEB have used its generic value  
 235 around 1.3 (Norman et al., 1995; Kustas and Norman, 1999; Bindlish et al., 2001; Anderson et  
 236 al., 2007; Colaizzi et al., 2014). Other studies have identified different values of  $\alpha_{PT}$  depending  
 237 on the vegetation cover fraction and particular forcing conditions. Notably, the PT coefficient  
 238 was found to be smaller for dry surfaces and higher for humid conditions (Eichinger et al.,  
 239 1996). Nevertheless the relative stability of  $\alpha_{PT}$  in many conditions has led to set  $\alpha_{PT}$  constant.  
 240 Consistent with this assumption,  $\alpha_{PT}$  is set to 1.26 in TSEB (Priestley and Taylor, 1972).

## 241 B. TSEB-SM model

242 The TSEB formalism is modified to integrate SM as an additional constraint on modeled  
 243 ET. In practice, the energy balance for vegetation and soil in TSEB-SM is the same as in TSEB,  
 244 but the soil evaporation is now explicitly represented as a function of SM via a soil resistance  
 245 term. Note that Song et al. (2016) have recently introduced SM in TSEB using a formulation  
 246 of soil evaporative efficiency. While there is partial equivalence between both formulations,  
 247 the soil resistance formulation is preferred herein as its parameters can be calibrated either from  
 248 soil texture information (Merlin et al., 2016) or from a combination of LST and SM data under  
 249 bare soil conditions (Merlin et al., 2017).

250 The soil latent heat flux is estimated as:

$$LE_{soil} = \frac{\rho c_p}{\gamma} \cdot \frac{(e_s - e_a)}{r_{ah} + r_s + r_{ss}} \quad (1)$$

251 where  $e_s$  is the saturated vapor pressure at the soil surface,  $e_a$  is the air vapor pressure, and  $r_{ss}$   
 252 is the resistance to vapor diffusion in the soil.  $r_{ss}$  is expressed as follows (Passerat de Silans,  
 253 1986) :

$$r_{ss} = \exp(a_{r_{ss}} - b_{r_{ss}} * \frac{SM}{SM_{sat}}) \quad (2)$$

254 with SM being the soil moisture in the 0-5 cm soil layer,  $a_{r_{ss}}$  and  $b_{r_{ss}}$  are two empirical  
 255 parameters and  $SM_{sat}$  the soil moisture at saturation expressed as:

$$SM_{sat} = 0.1 * (-108 * f_{sand} + 49.305) \quad (3)$$

256 with  $f_{sand}$  is the percentage of sand in the soil.

257 The flowchart of Figure 2 summarizes the different steps followed to resolve the energy balance  
 258 in TSEB-SM model. The algorithm is based on an iterative procedure that loops on the Monin-  
 259 Obukhov length (MO length), which is a scale parameter that characterizes the degree of  
 260 instability or stability of the boundary layer. MO length is approximately the height at which  
 261 aerodynamic shear, or mechanical energy, is equal to the buoyancy energy. In practice, MO  
 262 length is used as correction factor to determine the aerodynamic resistance  $r_{ah}$ . First, the  
 263 algorithm starts by initializing the soil and vegetation temperatures, as well as sensible and  
 264 latent heat fluxes. Then it calculates the available energy for the soil-vegetation-atmosphere  
 265 interface by estimating the surface net radiation and its partition between the vegetation and  
 266 the soil, as well as the soil heat flux. The way soil and vegetation temperatures are estimated is  
 267 in fact a specificity of the new model, which is based on the explicit resolution of the energy  
 268 balance for soil and vegetation respectively. Component temperatures are obtained by  
 269 minimizing cost functions  $F_{soil}$  and  $F_{veg}$ :

$$F_{soil,k} = (R_{n,soil,k} - H_{soil,k} - LE_{soil,k} - G_k)^2 \quad (4)$$

270



$$F_{\text{veg},k} = (R_{\text{n,veg},k} - H_{\text{veg},k} - LE_{\text{veg},k})^2 \quad (5)$$

271 with  $k$  being a loop index. By using the formula of the Newton method:

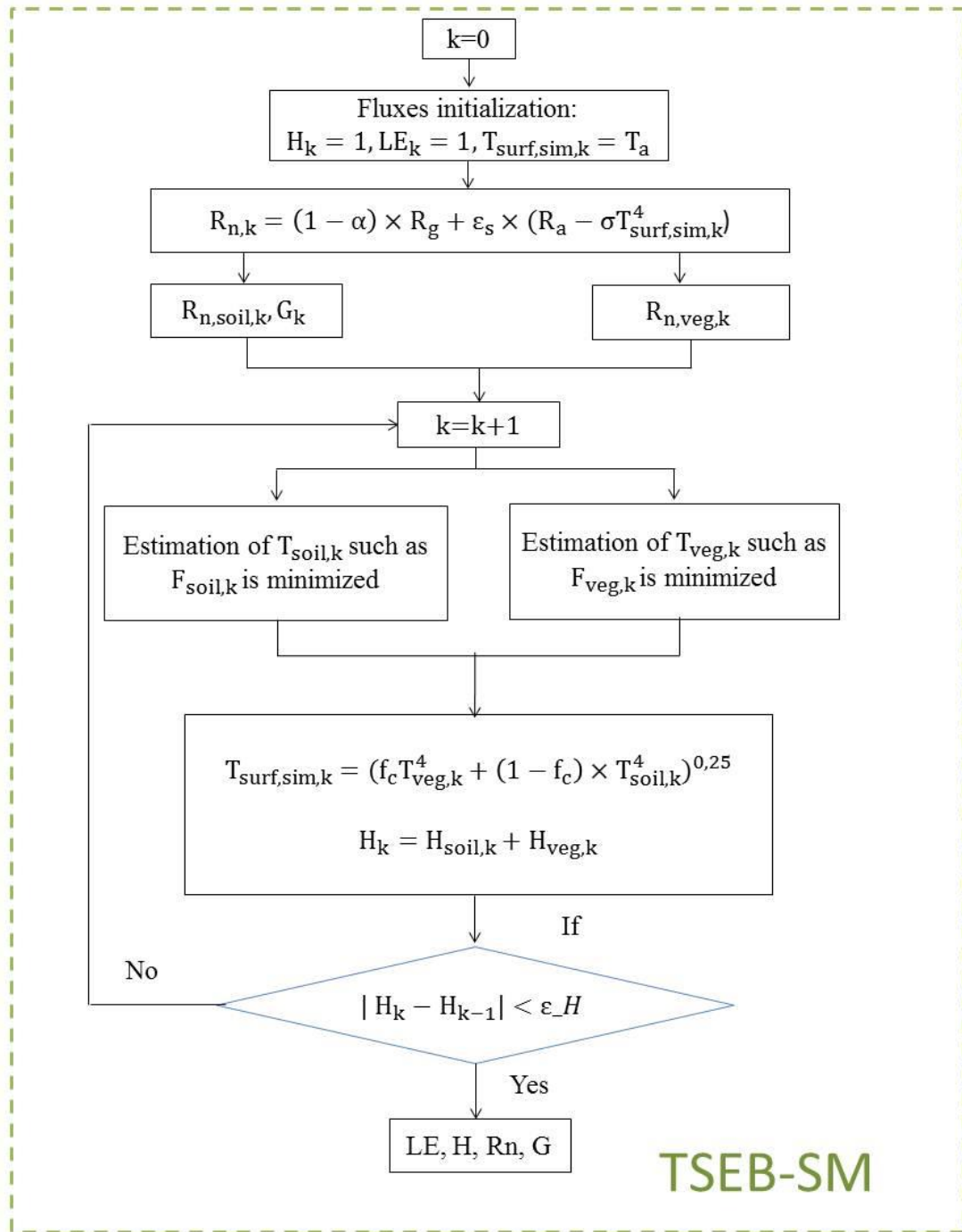
$$T_{\text{soil},k+1} = T_{\text{soil},k} - \frac{F_{\text{soil},k}}{dF_{\text{soil},k}} \quad (6)$$

$$T_{\text{veg},k+1} = T_{\text{veg},k} - \frac{F_{\text{veg},k}}{dF_{\text{veg},k}} \quad (7)$$

273 where  $dF_{\text{soil}}$  and  $dF_{\text{veg}}$  are the first derivative of the cost function for soil and vegetation,  
274 respectively.

275 At the end of each iteration, the simulated LST (noted  $T_{\text{surf},\text{sim}}$  Figure 2) and heat fluxes are  
276 used to recalculate the MO length iteratively. The iterative procedure is repeated until MO  
277 length (and  $H$ ) converges, meaning that the difference between two successive values is smaller  
278 than a given threshold (numerical uncertainty).

279



280  
281

Figure 2. Schematic diagram of TSEB-SM model.

282

### 283 2.2.2 Calibration strategies

284 The calibration approach of TSEB-SM is presented below. In this case, the calibration  
285 strategy is tightly coupled to the model formalism and the availability of input data (LST in the  
286 former case and both LST and SM in the latter).

## 287 C. TSEB-SM

288 The calibration procedure of TSEB-SM is presented in the schematic diagram of Figure  
 289 3. It is done in two steps: the first aims to provide first guess estimates of  $a_{r_{ss}}$  and  $b_{r_{ss}}$  (named  
 290  $a_{r_{ss},FG}$  and  $b_{r_{ss},FG}$ ) as input to the second step that aims to provide the final values of ( $a_{r_{ss},cal}$ ,  
 291  $b_{r_{ss},cal}$ ) and  $\alpha_{PT,cal,daily}$ .

292 Given that soil evaporation and plant transpiration may compensate each other to result in  
 293 similar total ET values, it is important to ensure that the calibration procedure is well defined,  
 294 meaning that a unique triplet ( $a_{r_{ss}}$ ,  $b_{r_{ss}}$ ,  $\alpha_{PT}$ ) is systematically obtained at the desired time scale.  
 295 In order to do so, the calibration data set is divided into two regions with specific behaviors: i)  
 296 data with  $f_c \leq 0.5$  for which ET is mainly controlled by soil evaporation and ii) data with  $f_c >$   
 297  $0.5$  for which ET is dominated by plant transpiration. In both data sets, soil evaporation and  
 298 plant transpiration may occur simultaneously but the LST over the mixed surface is expected  
 299 to be more sensitive to soil evaporation and plant transpiration for  $f_c \leq 0.5$  and  $f_c > 0.5$ ,  
 300 respectively (Moran et al. 1994; Merlin et al. 2012).

301 The first calibration step initializes  $\alpha_{PT}=1.26$  and inverts  $r_{ss}$  at each time (30-min) step for data  
 302 with  $f_c \leq 0.5$ . The  $r_{ss}$  is first adjusted to minimize the following cost function:

$$F_{inst} = (T_{surf,sim} - T_{surf,mes})^2 \quad (8)$$

303 using the Newton method:

$$r_{ss,k+1} = r_{ss,k} - \frac{F_{instk}}{dF_{instk}} \quad (9)$$

304 where  $T_{surf,sim}$  and  $T_{surf,mes}$  are the LST simulated by TSEB-SM model and observed over the  
 305 crop field at the 30-min time step, respectively. The inverted  $r_{ss}$  is then correlated to the  
 306 observed SM to estimate  $a_{r_{ss}}$  and  $b_{r_{ss}}$ . In practice,  $a_{r_{ss}}$  and  $-b_{r_{ss}}/SM_{sat}$  are the intercept and the  
 307 slope of the linear regression of the  $\ln(r_{ss})$  versus SM relationship (see Equation 2). As the  
 308 retrieved pair ( $a_{r_{ss}}$ ,  $b_{r_{ss}}$ ) depends on the  $\alpha_{PT}$  value, an iterative loop is run on  $a_{r_{ss}}$ ,  $b_{r_{ss}}$  and  $\alpha_{PT}$   
 309 until convergence of  $a_{r_{ss}}$  and  $b_{r_{ss}}$  is achieved. At each iteration, the inverted  $a_{r_{ss}}$  and  $b_{r_{ss}}$  are used  
 310 as input to invert  $\alpha_{PT}$  for data with  $f_c > 0.5$ . The PT Taylor coefficient is adjusted, at the daily  
 311 time scale, to minimize the following cost function:

$$F_{daily} = \sum_{i=1}^N (T_{surf,sim,i} - T_{surf,mes,i})^2 \quad (10)$$

312 with N being the number of 30-min LST measurements available for a given day. To keep a  
 313 (time) scale consistency between all three retrieved parameters in calibration step 1, the daily  
 314 inverted  $\alpha_{PT}$  is averaged at the seasonal time scale before being used as input to the following  
 315 (next iteration) inversion of  $a_{r_{ss}}$  and  $b_{r_{ss}}$ . To further assess the model's stability, the initial values  
 316 of ( $a_{r_{ss},k=0}$ ,  $b_{r_{ss},k=0}$ ) were randomly set to a range of values between 1 and 13 and the results (not  
 317 shown) confirmed the robustness of the calibration approach, regardless of the initialization.

318 The second calibration step refines the estimation of  $\alpha_{PT}$  at the daily scale. The first guess  $a_{r_{ss},FG}$   
 319 and  $b_{r_{ss},FG}$  obtained in step 1 are first used as input to the retrieval procedure of daily  $\alpha_{PT}$  for  
 320 data with  $f_c > 0.5$  (minimization of  $F_{daily}$ ). Next, the daily retrieved  $\alpha_{PT}$  is smoothed to remove  
 321 outliers as well as to reduce random uncertainties in daily retrieved  $\alpha_{PT}$ . Then, the smoothed  
 322  $\alpha_{PT}$  is normalized between its minimum and maximum values reached during the agricultural  
 323 season after having forced the minimum value of smoothed  $\alpha_{PT}$  to 0 at harvest so that  
 324 transpiration is zero at this time:

$$\alpha_{PT,cal,daily} = \frac{\alpha_{PT,daily,smooth} - \min(\alpha_{PT,daily,smooth})}{\max(\alpha_{PT,daily,smooth}) - \min(\alpha_{PT,daily,smooth})} * \max(\alpha_{PT,daily,smooth}) \quad (11)$$

325 Finally  $r_{ss}$  is calibrated a last time to ensure consistency between daily calibrated  $\alpha_{PT,cal,daily}$   
 326 and final  $a_{rss,cal}$  and  $b_{rss,cal}$  (see Figure 3).  
 327

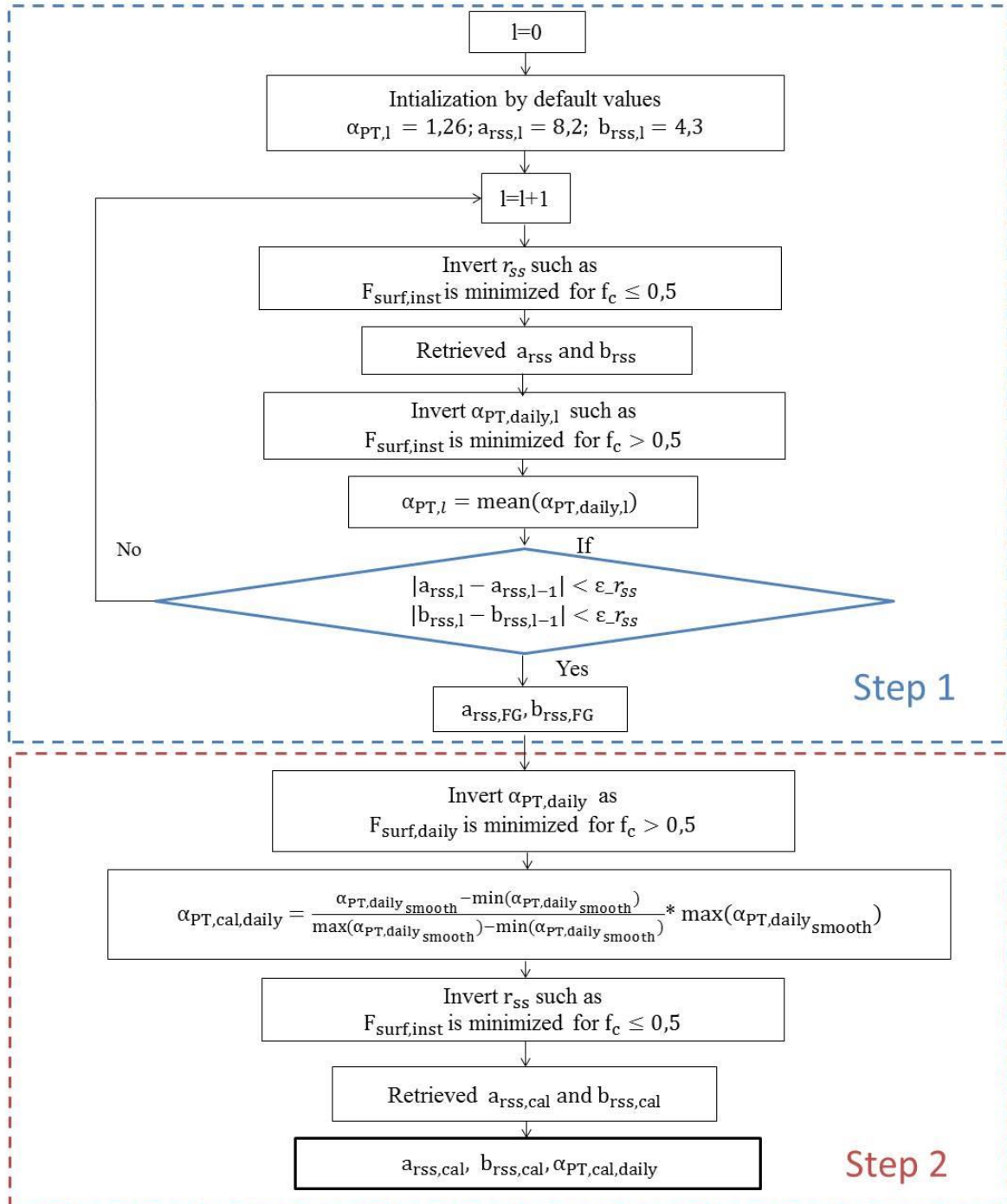


Figure 3. Schematic diagram of the two-step calibration strategy of TSEB-SM model.

328  
 329

330

### 331 **3 Results and Discussions**

332 The proposed calibration of  $r_{ss}$  and  $\alpha_{PT}$  is successively applied to the flood-irrigated (R3),  
333 the controlled drip-irrigated (Chichaoua) and the reference drip-irrigated (Chichaoua) wheat  
334 sites. The TSEB-SM approach is then assessed in terms of evapotranspiration. In practice, the  
335 H and LE simulated at the half hourly time scale (between 11 am and 1:30 pm) by TSEB-SM  
336 and by the original TSEB model (using an a priori default value for  $\alpha_{PT}$ ) are compared against  
337 EC measurements at the three experimental sites.

#### 338 5.1 Retrieved parameters

339 Figure 4 plots the iterative values of  $a_{rss}$ ,  $b_{rss}$  and mean  $\alpha_{PT}$  during calibration step 1.  
340 Iteration 0 corresponds to default values. The convergence of all three parameters is very fast,  
341 requiring only 2 or 3 iterations for achieving a relative error better than 1%. This result confirms  
342 the appropriateness of separating the calibration range in  $f_c$  intervals where one parameter has  
343 significantly more weight on simulation results (i.e. simulated LST and associated fluxes) than  
344 the others. The calibrated pair ( $a_{rss}$ ,  $b_{rss}$ ) is (5.67, 1.40), (6.51, 3.82) and (9.47, 6.87) for the  
345 flood-, controlled drip- and reference drip-irrigated field, respectively. The mean retrieved  
346 values (7.2, 4.0) are relatively close to those estimated in Sellers et al. (1992) (8.2, 4.3). The  
347 variability of  $a_{rss}$  and  $b_{rss}$  can be explained by numerous factors such as soil texture (Merlin et  
348 al., 2016) and meteorological conditions (Merlin et al., 2011). Nevertheless, retrieved  
349 parameters are significantly different for both drip sites whereas they i) are located about 200  
350 m apart only and ii) have similar soil texture and meteorological conditions. In fact, retrieved  
351  $a_{rss}$  is an increasing function of retrieved  $b_{rss}$  due to compensation effects between  $a_{rss}$  and  $b_{rss}$   
352 for a given SM and LST observation pair and regardless of soil properties and meteorological  
353 conditions. Such compensation reveals the empirical nature of the  $r_{ss}$  formulation in Sellers et  
354 al. (1992).

355

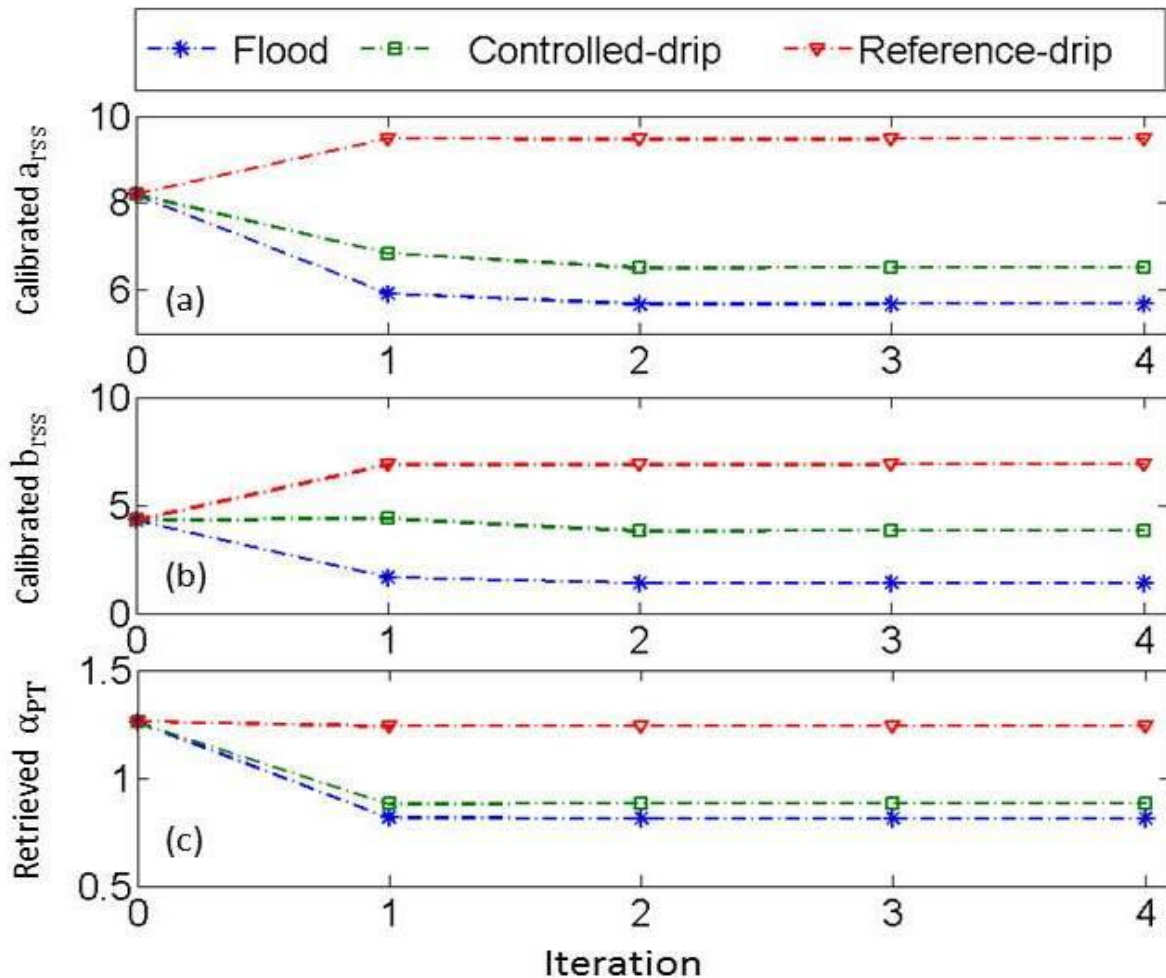


Figure 4. Iterative values of  $a_{RSS}$ , (a),  $b_{RSS}$  (b) and mean value of retrieved  $\alpha_{PT}$  (c) for the flood-, controlled drip- and reference drip-irrigated wheat fields separately (calibration step 1).

356  
357  
358

359

360

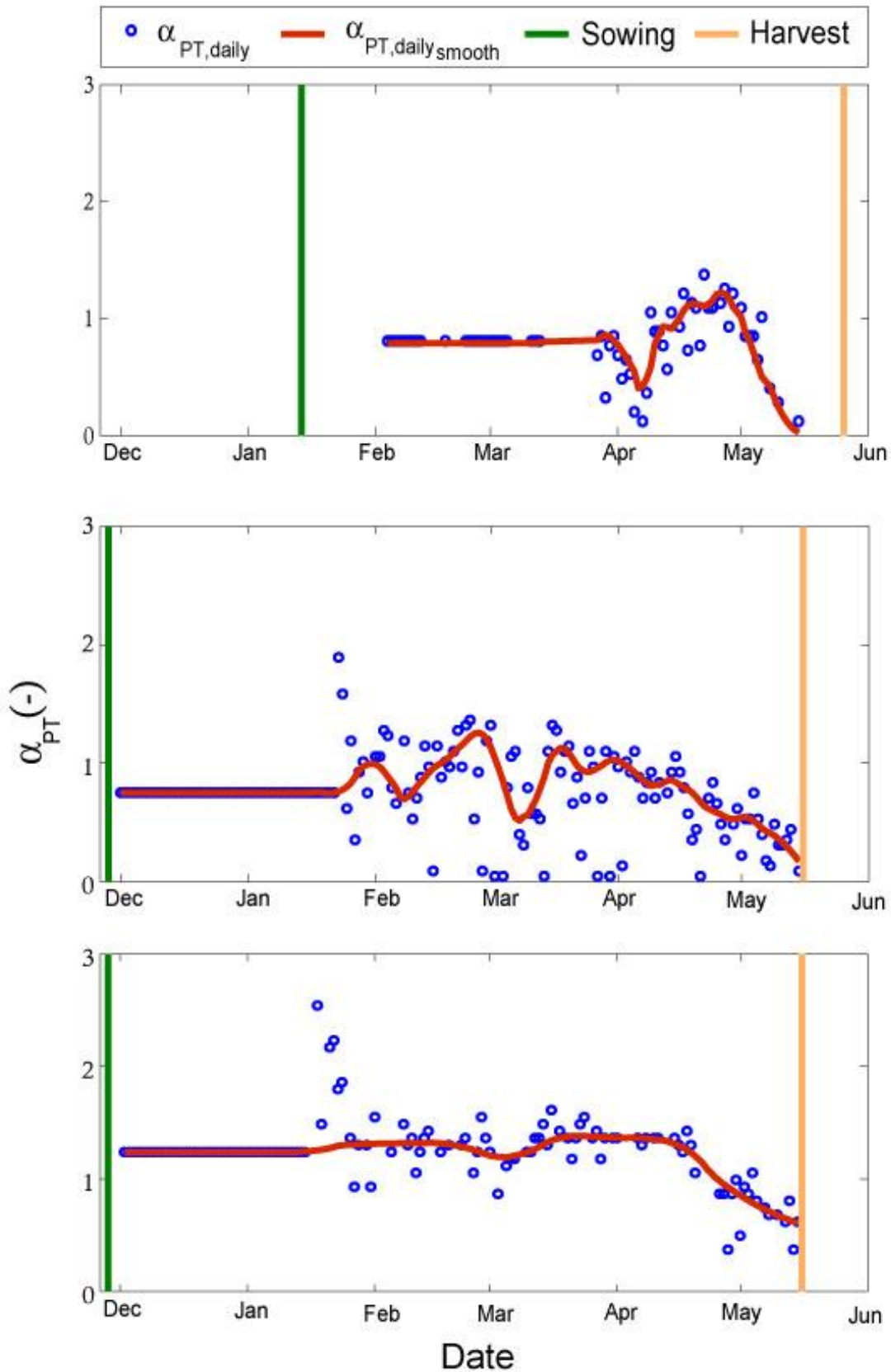
361 The mean value of  $\alpha_{PT}$  at the semi-hourly time scale (see Figure 4) is 0.81, 0.88 and 1.24 for  
362 the flood-, controlled drip- and reference drip-irrigated wheat fields, respectively. Note that the  
363 mean value is very close to the theoretical  $\alpha_{PT}$  value for the reference drip-irrigated field case.  
364 It is suggested that  $f_g$  generally equals 1 at the maximum of  $\alpha_{PT}$  (peak of ET), so that the  
365 maximum  $\alpha_{PT}$  value is directly comparable to its default value (1.26) corresponding to fully  
366 unstressed conditions (Priestley and Taylor, 1972). Nonetheless, the mean  $\alpha_{PT}$  is significantly  
367 smaller than the default value for the flood- and controlled drip-irrigated cases. Lower values  
368 can be associated with stress conditions that may have occurred during the crop development.

369 Figure 5 plots the time series of daily retrieved  $\alpha_{PT}$  for each site separately. It can be seen that  
370 the maximum value of daily  $\alpha_{PT}$  varies from field to field. It is estimated as 1.8, 2.10 and 2.82  
371 for the flood-, controlled drip- and reference drip-irrigated fields, respectively. It is clearly  
372 observed that the values related to drip irrigation are significantly greater than the values related  
373 to flood irrigation. This could be explained by the difference in agricultural practices of each  
374 field (sowing date, irrigation events, rainfall and fertilization) as well as uncertainties in  
375 retrieved  $\alpha_{PT}$ . Two effects are likely to explain the highly variable and excessively high  
376 retrieved  $\alpha_{PT}$  values over the drip irrigated site for the first few daily retrievals. First, it is  
377 reminded that  $\alpha_{PT}$  is retrieved for  $fc > 0.5$ . When  $fc$  is slightly larger than 0.5 (that is on the first

378 few retrieval days of the season), large uncertainties in retrieved  $\alpha_{PT}$  are expected because the  
379 soil surface still plays a significant role in the observed LST. Little response is shown for the  
380 first two months over the flood irrigation field, because the flux measurements over this site  
381 started when wheat was already well developed ( $f_c$  significantly larger than 0.5). Second, the  
382 R3 site is surrounded by homogeneous irrigated wheat fields while the drip irrigated fields are  
383 surrounded by dryland, which potentially reinforces advection effects, leading to enhanced  
384 retrieved  $\alpha_{PT}$ . Note that the retrieved  $\alpha_{PT}$  values above 2 and near 0 are due to the uncertainties  
385 in LST-derived daily estimates, especially during the periods when wheat is partially covering  
386 the soil.

387 As explained above, a smoothing function is applied to reduce uncertainties in daily  $\alpha_{PT}$ . The  
388 smoothing length (it is one parameter of the smoothing function) is set to 10% of the total time  
389 series, that is about 10-20 days. Such a smoothing procedure is justified by the fact that both  
390 biomass and root-zone soil moisture commonly change across the agricultural season with a  
391 characteristic time of 1 to 2 weeks (Albergel et al. 2008). Furthermore, Figure 5 clearly shows  
392 that the smoothing function removes all outliers while capturing significant patterns at the quasi  
393 daily scale. The smoothed  $\alpha_{PT}$  ranges from 0.03 to 1.22, 0.17 to 1.26 and 0.61 to 1.38 for the  
394 flood-, controlled drip- and reference drip-irrigated wheat, respectively.

395



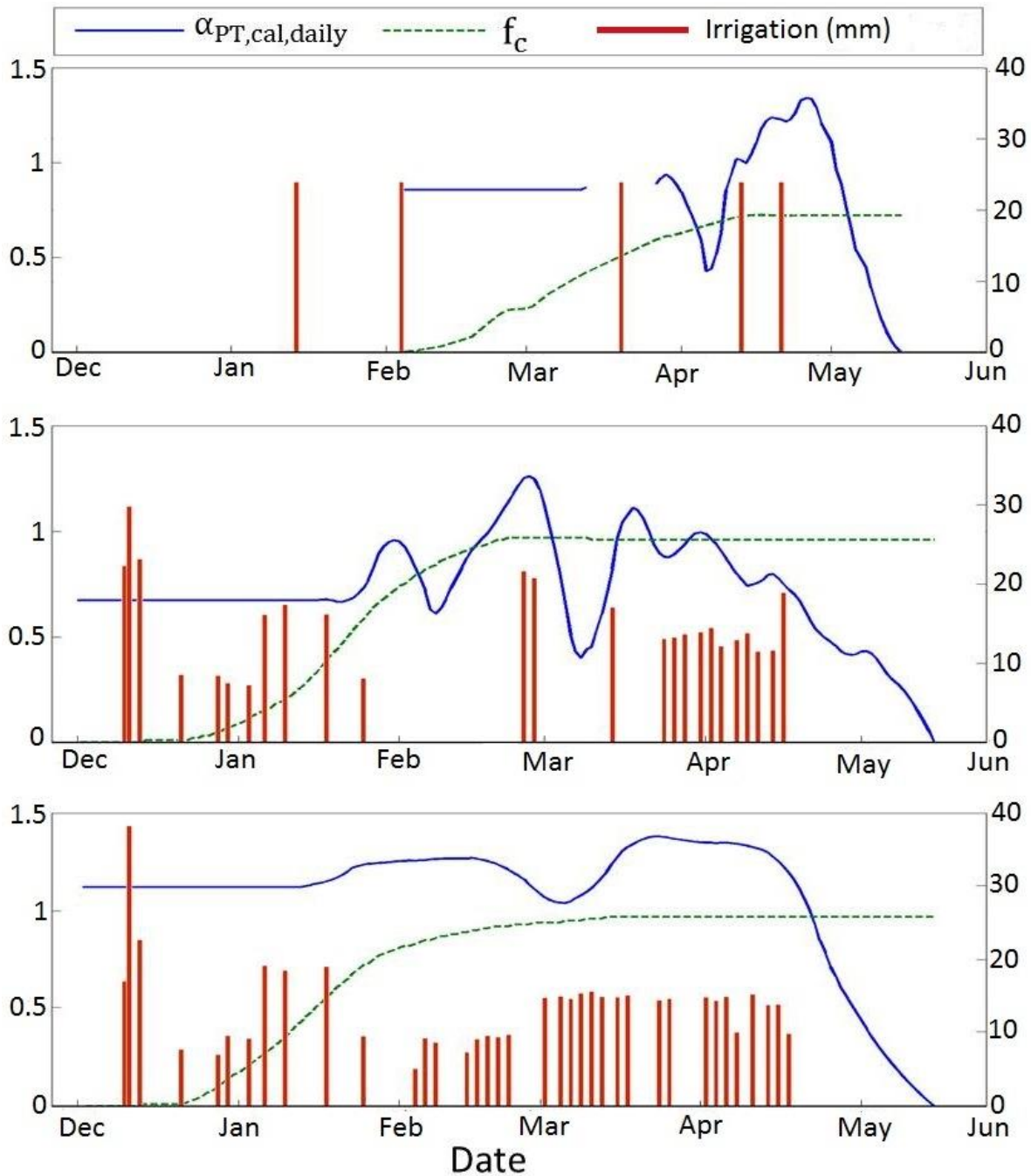
396  
397  
398

Figure 5. Time series of daily retrieved and smoothed  $\alpha_{PT}$  for the (a) flood-, (b) controlled drip- and (c) reference drip-irrigated wheat fields, separately (calibration step 2).

399



400 The normalization in Equation (11) of smoothed  $\alpha_{PT}$  between its assumed minimum value (0)  
401 and smoothed maximum value makes the calibrated daily  $\alpha_{PT}$  range from 0 to 1.22, 0 to 1.26  
402 and 0 to 1.38 for the flood-, controlled drip- and reference drip-irrigated fields, respectively.  
403 Time series of calibrated daily  $\alpha_{PT}$  are presented in Figure 6 superimposed with  $f_c$  for  
404 comparison purposes. The maximum calibrated daily  $\alpha_{PT}$  is close to the theoretical value of  
405 1.26 in each case. However, its temporal variability is found to be significant even during the  
406 growing stage of wheat. Calibrated daily  $\alpha_{PT}$  is more stable for the reference drip field than for  
407 both flood and controlled drip fields, with a relative change during the growing period of 8.08%  
408 compared to 26.94% and 22.66% for the other two fields, respectively. This result is consistent  
409 with the fact that the reference drip field had been irrigated according to the water needs  
410 estimated by the FAO-56 method while the other two fields (flood and controlled drip) had  
411 been under water deficit conditions for one or several periods during the growing stage. Note  
412 that the controlled-drip field has a special feature in terms of  $\alpha_{PT}$  daily dynamics. The maximum  
413 value is reached by the beginning of March, which is much earlier than the  $\alpha_{PT}$  peak observed  
414 at the reference drip (around late April) and flood (beginning of May) fields, although wheat  
415 was sowed on the same date as reference drip field. It is suggested that the controlled drip-  
416 irrigated wheat did not recover well from the first (relatively long) stress period from  
417 22/02/2017 to 06/03/2017. The irrigation water supplied after mid-March was probably not  
418 sufficient for the wheat of controlled drip field to catch up with the reference drip-irrigated  
419 wheat, even if the amount of water used for irrigation after this period was approximately the  
420 same (about 166 mm).  
421



422  
423  
424

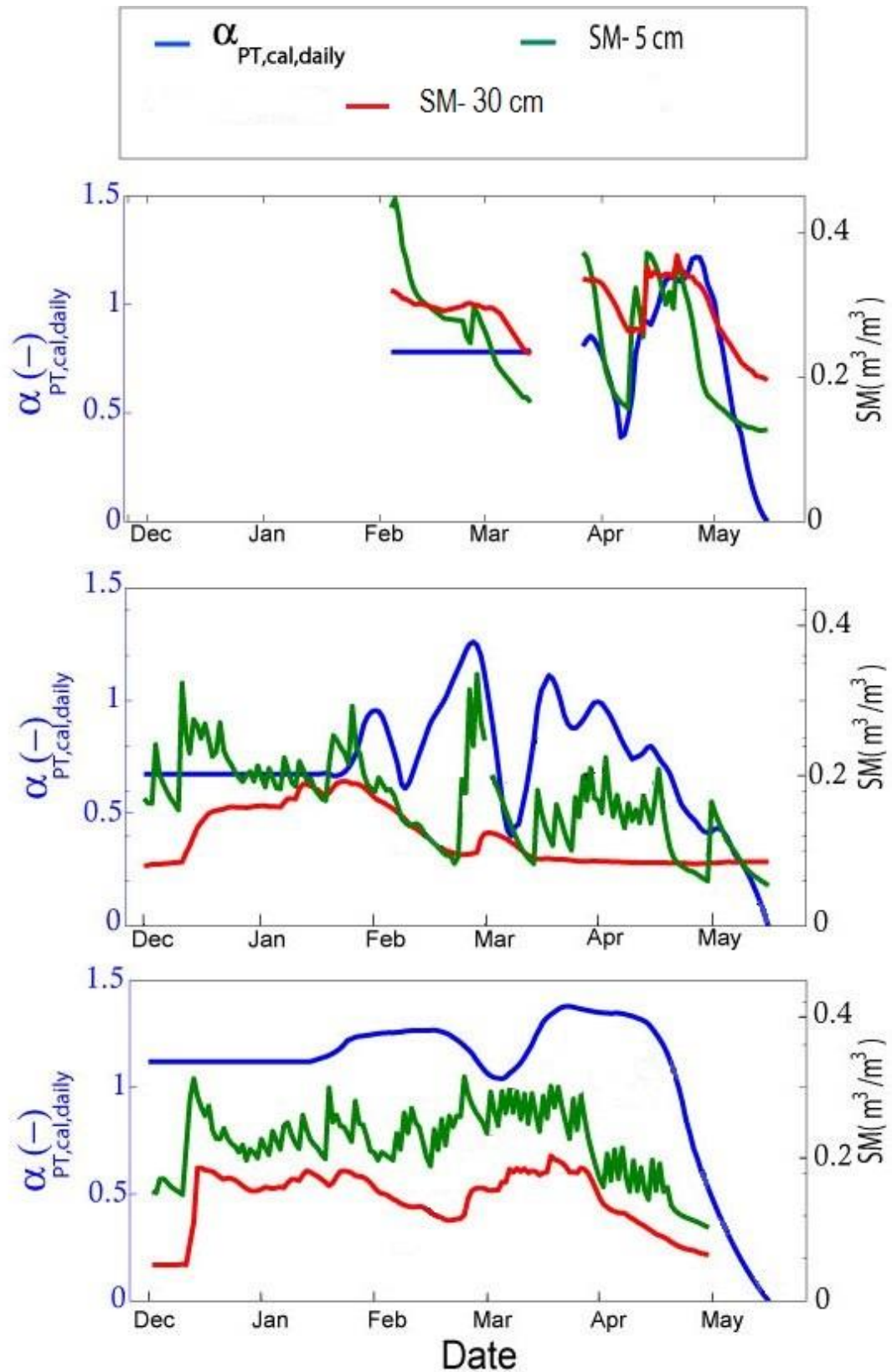
Figure 6. Time series of calibrated daily  $\alpha_{PT}$ , superimposed with  $f_c$  for the (a) flood-, (b) controlled drip- and (c) reference drip-irrigated wheat fields, separately. The red segments represent irrigations during the season.

425

## 426 5.2 Interpretation of $\alpha_{PT}$ variabilities

427  $\alpha_{PT}$  is expected to vary according to several factors including LAI, green fraction cover and  
 428 soil water availability. In order to verify the consistency of the variations in daily retrieved  $\alpha_{PT}$ ,  
 429 Figure 7 presents the time series of calibrated daily  $\alpha_{PT}$  superimposed with near-surface (5-cm)  
 430 soil moisture, deeper (30-cm) soil moisture. It is reminded that the daily  $\alpha_{PT}$  for  $f_c < 0.5$  is set  
 431 to the mean daily  $\alpha_{PT}$  obtained for  $f_c > 0.5$  (see Figure 6). Therefore, the variability of  $\alpha_{PT}$  should  
 432 be interpreted for  $f_c > 0.5$  only, that is from  $f_c = 0.5$  until harvest. Figure 7 illustrates the expected  
 433 relationships between  $\alpha_{PT}$  and the water availability in the soil column. In each case, the  $\alpha_{PT}$   
 434 dynamics are driven by soil moisture variations.

435 The qualitative analysis of  $\alpha_{PT}$  variability in relation to soil water availability indicates that  $\alpha_{PT}$   
436 cannot be considered as a constant. Large variations in this parameter are likely to occur during  
437 the agricultural season, especially under stress conditions. Water deficit may happen with flood  
438 irrigation when the frequency of water supplies (every 3 weeks on average over R3) is  
439 relatively low compared to the water demand under such semi-arid conditions. Indeed the water  
440 stress observed in the flood-irrigated wheat may be attributed to the increase in water depletion  
441 at the root zone through a removal of water by transpiration and percolation losses (Er-Raki et  
442 al., 2007). Water stress may also happen with drip when the technique is not appropriately  
443 implemented or by applying regulated deficit irrigation.  
444



445  
446  
447

Figure 7. Time series of  $\alpha_{PT,cal,daily}$  superimposed with 5-cm/30-cm soil moisture (SM) for: (a) flood-, (b) controlled drip- and (c) reference drip-irrigated fields, respectively.

448

## 449 5.3 Surface fluxes

450 The ability of TSEB and TSEB-SM for partitioning the available energy into H and LE  
451 is assessed by forcing -in each case-  $R_n$  and G to their measured values. Note that the calibration  
452 of TSEB-SM is still undertaken using observed LST, SM and  $f_c$  whereas the validation of TSEB  
453 and TSEB-SM model output is undertaken using EC measurements of H and LE. The metrics  
454 used to evaluate results comprise the determination coefficient ( $R^2$ ), the root mean square error  
455 (RMSE) and the mean bias error (MBE) between simulated and observed fluxes.

456 Figure 8 plots simulated versus observed LE for the three sites separately. TSEB provides  
457 satisfying results for the flood site with a RMSE of  $78 \text{ W/m}^2$  and a relative error (estimated as  
458 RMSE divided by mean observed LE) of 27%. However, two notable features are observed for  
459 the other two (controlled and reference drip) sites: i) the LE simulated by TSEB never exceeds  
460  $500 \text{ W/m}^2$  over the entire growing season ( $f_c > 0.5$ ) although observations reach  $700 \text{ W/m}^2$  and  
461 ii) the overall MBE is about  $29 \text{ W/m}^2$  and  $66 \text{ W/m}^2$  for the controlled and reference drip field  
462 respectively, meaning that TSEB also overestimates LE in the lower ET range. To dig deeper,  
463 the performance of TSEB is now assessed by analyzing the metrics computed for three distinct  
464 periods of the agricultural season: the period for  $f_c \leq 0.5$ , for  $f_c > 0.5$  and the senescence  
465 stage. Note that the senescence period is defined herein as starting after the last peak observed  
466 on the calibrated daily  $\alpha_{PT}$  (becomes remarkable after about one week) and finishing when  
467 green fraction cover becomes zero, which corresponds to the last date of the three time series.  
468 Hence the senescence starts on 27/04/2003, 19/04/2017 and 15/04/2017 for the flood-,  
469 controlled drip- and reference drip-irrigated field, respectively. A visual assessment of scatter  
470 plots in Figure 8 and the statistics presented in Table 1 clearly indicate that TSEB  
471 underestimates LE fluxes at around the maximum of ET (well developed crop before  
472 senescence) while it overestimates LE fluxes during senescence until harvest. The saturation  
473 of TSEB in the higher range of ET is due to the fixed maximum value for  $\alpha_{PT}$  (equal to 1.26).  
474 The structure of the model cannot accommodate large evaporative demand conditions and  
475 strong advective conditions (Song et al., 2016).

476 Both limitations identified in the TSEB formalism seem to be partly solved by the TSEB-SM  
477 approach. In particular, the LE simulated by TSEB-SM (Figure 8) is closer to the 1:1 line in  
478 each case ( $f_c \leq 0.5$  and  $f_c > 0.5$  and the senescence), providing a quite significant  
479 improvement for drip sites. The simulated LE does not saturate as it reaches  $700 \text{ W/m}^2$  over  
480 the reference drip site. In fact, the retrieval of daily  $\alpha_{PT}$  values larger than the theoretical  
481 maximum 1.26 significantly improves ET estimates. Moreover, the overestimation of LE  
482 during the senescence stage is much reduced for TSEB-SM. It is suggested that the decrease in  
483 calibrated daily  $\alpha_{PT}$  integrates the drop in green vegetation fraction that takes place during  
484 senescence.

485

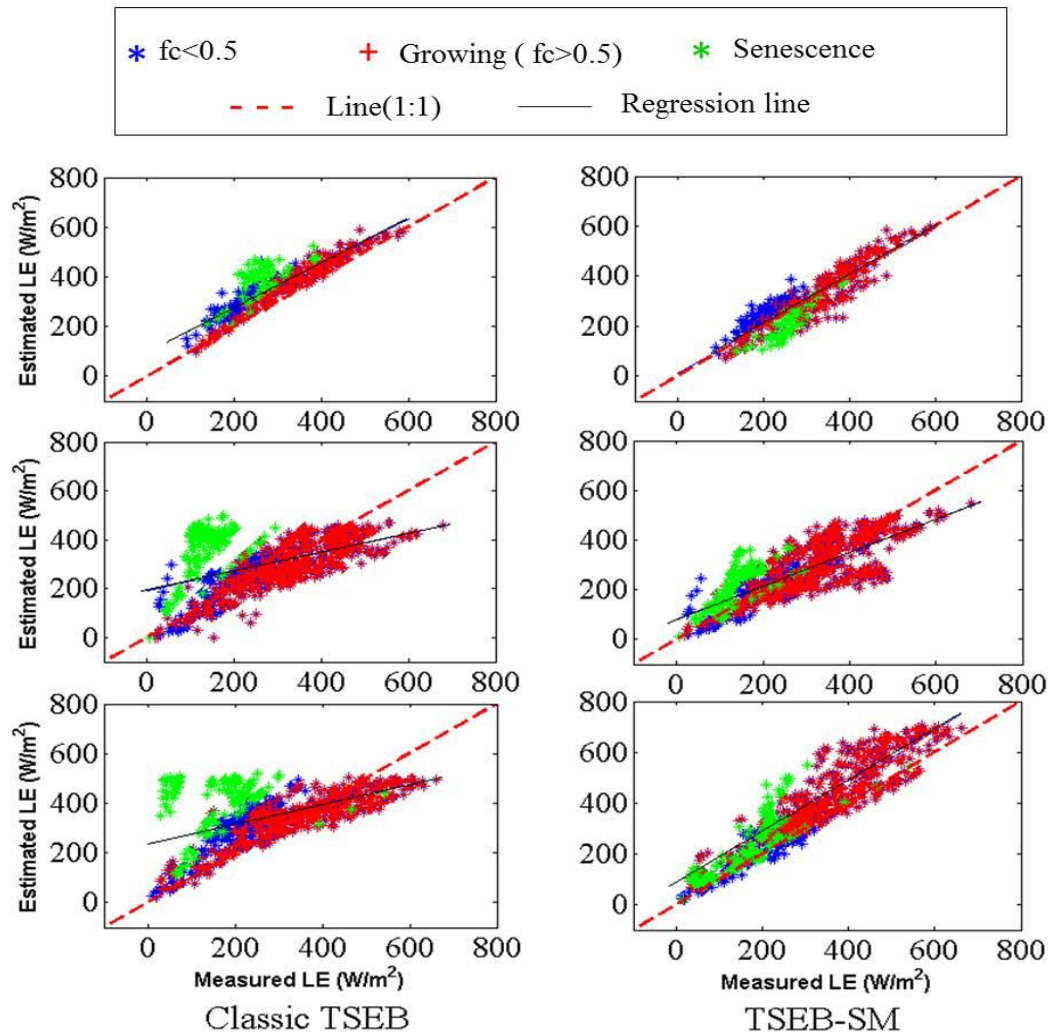


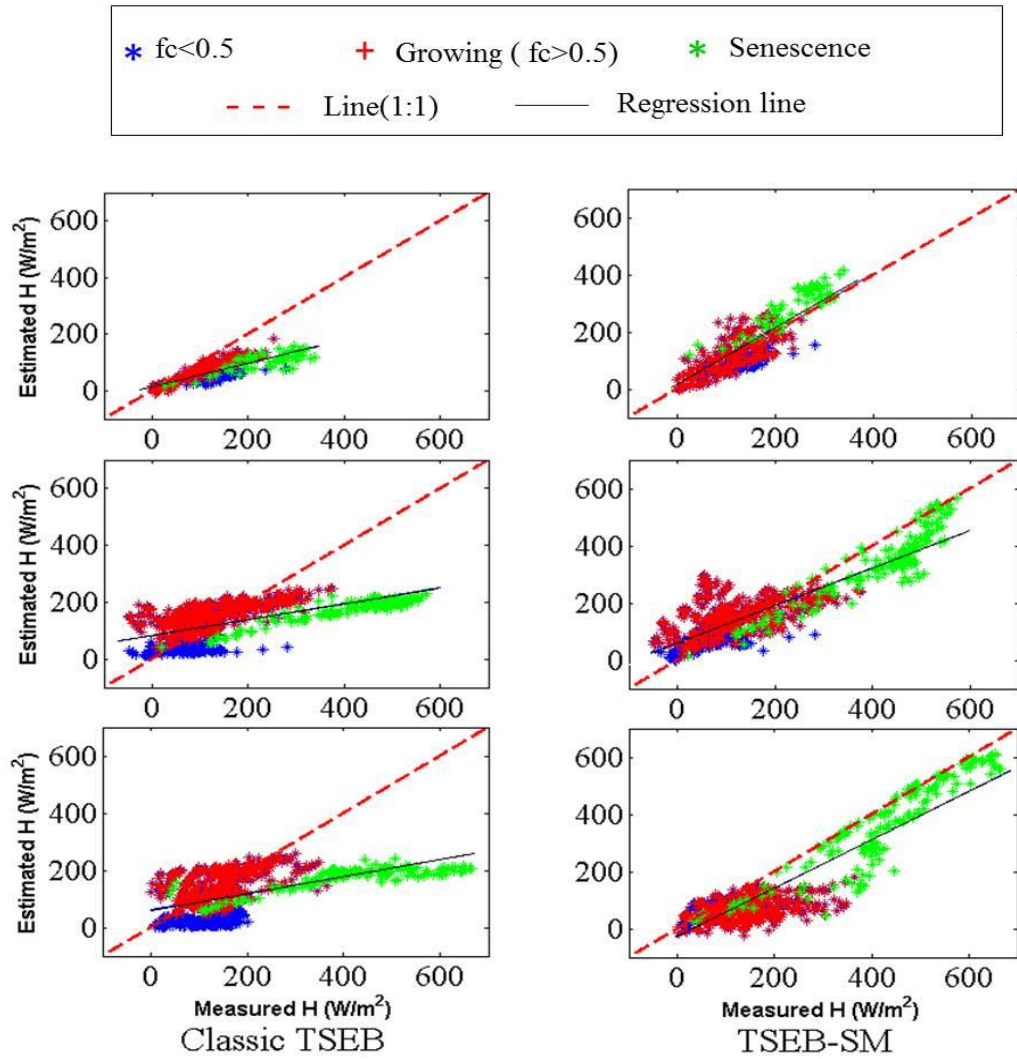
Figure 8. Scatterplot of simulated versus observed LE for the (top) food-, (middle) controlled drip- and (bottom) reference drip-irrigated fields and for (left) TSEB-SM and (right) TSEB models, respectively.

486  
487  
488

489

490 The comparison between TSEB and TSEB-SM is continued by plotting simulated versus  
491 observed H for each site in Figure 9. Consistent with previous results obtained for LE, the  
492 calibration strategy within TSEB-SM provides in general a significantly improved RMSE  
493 compared to the original TSEB. The RMSE is 49 W/m<sup>2</sup> instead of 73 W/m<sup>2</sup>, 78 W/m<sup>2</sup> instead  
494 of 78 W/m<sup>2</sup> and 119 W/m<sup>2</sup> instead of 128 W/m<sup>2</sup> for the flood-, controlled drip- and reference  
495 drip-irrigated field respectively. The determination coefficient between simulated and observed  
496 H is significantly improved from 0.61 to 0.67, from 0.37 to 0.75 and from 0.29 to 0.82,  
497 respectively when including calibrated parameters to TSEB-SM.

498 One can observe that the slope of the linear regression between TSEB and in situ H is very low  
499 in all cases. The modeled H does not seem to be sensitive enough to changes in surface and  
500 atmospheric conditions during all three periods ( $f_c \leq 0.5$ ,  $f_c > 0.5$  and senescence).  
501



502

503

504 *Figure 9. Scatterplot of simulated versus observed H for the (top) flood-, (middle) controlled drip- and (bottom) reference*  
 505 *drip-irrigated fields and for (right) TSEB and (left) TSEB-SM model, respectively.*

506 **Tableau 1:** Error statistics (RMSE,  $R^2$  and MBE) between modeled and measured sensible and latent  
 507 heat fluxes for the flood, controlled drip- and reference drip-irrigated fields, and for TSEB and TSEB-  
 508 SM model, separately (Rn and G are forced to their measured value)

		TSEB-SM			TSEB		
		RMSE (W/m <sup>2</sup> )	R <sup>2</sup> (-)	MBE (W/m <sup>2</sup> )	RMSE (W/m <sup>2</sup> )	R <sup>2</sup> (-)	MBE (W/m <sup>2</sup> )
Latent heat flux (LE)	Flood	49	0.79	-4	78	0.79	66
	Controlled drip	73	0.64	-6	119	0.22	29
	Reference drip	78	0.86	56	128	0.28	66
Sensible heat flux (H)	Flood	49	0.67	4	78	0.61	-66
	Controlled drip	73	0.75	7	119	0.37	-29
	Reference drip	78	0.82	-56	128	0.29	-66

509

510

511 The intercomparison between TSEB and TSEB-SM is finally undertaken by simulating the  
 512 available energy, instead of forcing Rn and G to their measured values as in Table 1. Table 2  
 513 reports the error statistics for the four energy fluxes separately. The larger discrepancies for LE  
 514 estimated from TSEB-SM model in this case is likely due to greater scatter between modeled  
 515 and measured Rn, which is related to the difference between simulated and observed LST. Note  
 516 also that the determination coefficient between simulated and measured G is about 0.4-0.5 for  
 517 both TSEB and TSEB-SM and all three sites. This is linked in part to the relatively small  
 518 magnitude and range in the observed values combined with the simplicity of the approach used  
 519 to estimate G. Overall, the simulations of LE and H when modeling Rn and G are fully  
 520 consistent with those obtained when forcing Rn and G to their measured values. TSEB-SM still  
 521 provides superior results to TSEB in terms of RMSE, R<sup>2</sup> and MBE between simulated and  
 522 observed fluxes. Especially the sensible heat flux is significantly improved in all cases.

523

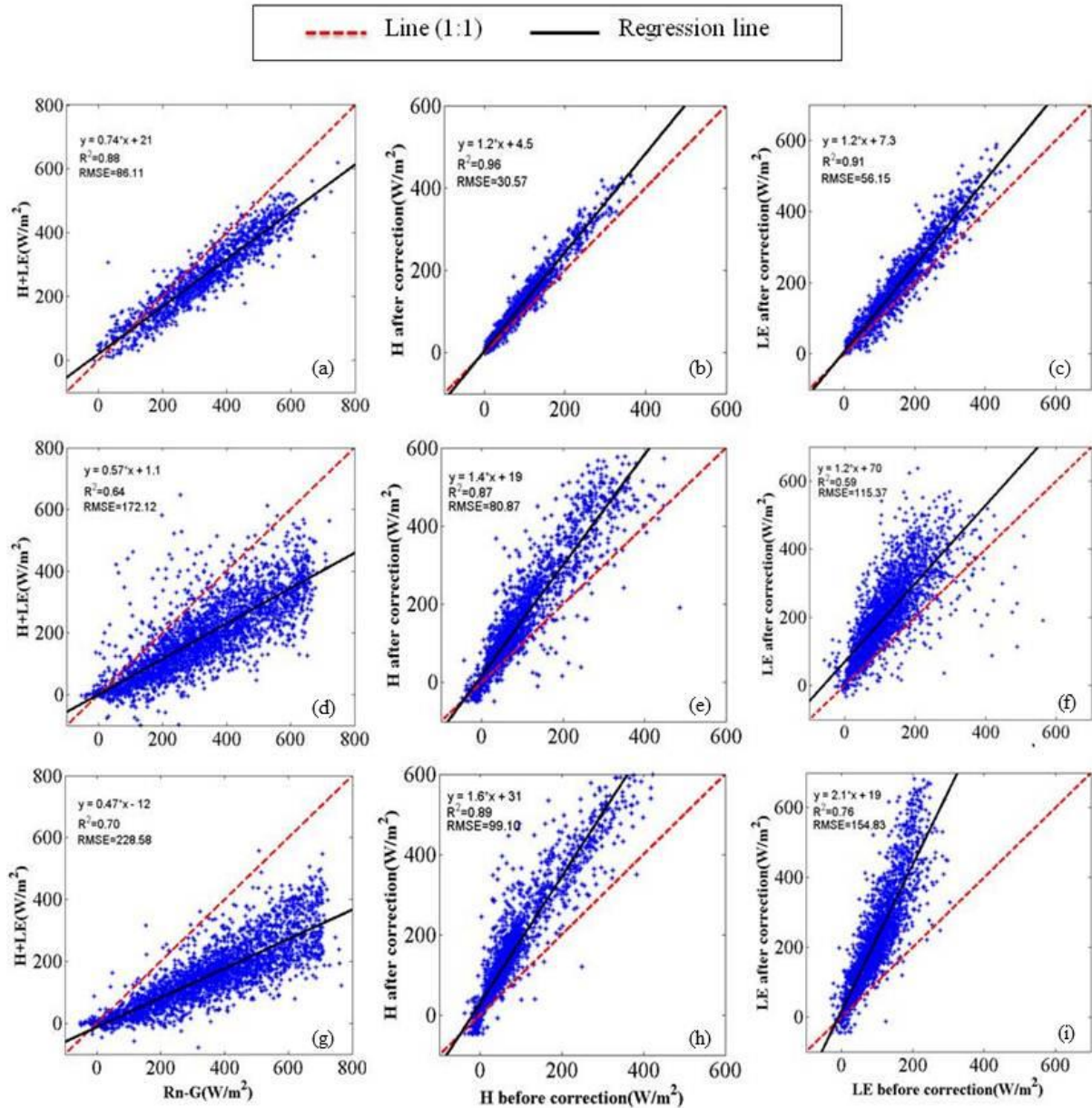
524 Tableau 2: Error statistics (RMSE, R<sup>2</sup> and MBE) between modeled and measured net radiation,  
 525 conductive flux, and sensible and latent heat fluxes for the flood, controlled drip- and reference drip-  
 526 irrigated fields, and for TSEB and TSEB-SM model, separately.

		TSEB-SM			TSEB		
		RMSE (W/m <sup>2</sup> )	R <sup>2</sup> (-)	MBE (W/m <sup>2</sup> )	RMSE (W/m <sup>2</sup> )	R <sup>2</sup> (-)	MBE (W/m <sup>2</sup> )
Net radiation (Rn)	Flood	31	0.98	-25	18	0.99	-17
	Controlled drip	27	0.98	-10	16	0.99	1
	Reference drip	50	0.95	-32	9	0.99	1
Conductif flux (G)	Flood	23	0.41	2	22	0.43	1
	Controlled drip	20	0.5	9	25	0.48	12
	Reference drip	14	0.39	14	30	0.38	26
Sensible heat flux (H)	Flood	27	0.66	34	78	0.61	-67
	Controlled drip	61	0.82	8	118	0.38	-28

527

528





529  
530 *Figure 10. Scatterplot of observed  $H+LE$  versus observed  $Rn-G$  (left), corrected  $H$  versus observed  $H$  (center) and corrected*  
531  *$LE$  versus observed  $LE$  (right) the food- (top), controlled (middle) and reference drip-irrigated (bottom) fields respectively.*

532

#### 533 4 Conclusions

534 A new evapotranspiration model named TSEB-SM is derived from the TSEB formalism by  
535 explicitly representing soil evaporation using a soil resistance. An innovative calibration  
536 approach is also developed to retrieve the main parameters of soil evaporation and plant  
537 transpiration via the soil resistance and  $\alpha_{PT}$  respectively. In practice the soil resistance  
538 parameters are retrieved at the seasonal time scale from SM and LST data with  $f_c \leq 0.5$ . While  
539  $\alpha_{PT}$  is retrieved at the daily time scale from SM and LST data for  $f_c > 0.5$ . The performance  
540 of TSEB-SM and TSEB models is assessed in terms of  $LE$  and  $H$  partitioning using an in situ  
541 data set collected over 1 flood- and 2 drip-irrigated wheat fields.

542 The convergence of the iterative calibration procedure on  $(a_{r_{ss}}, b_{r_{ss}})$  and  $\alpha_{PT}$  is successfully  
543 tested when all three parameters are estimated at the seasonal time scale, as well as when

544 considering a daily variability of  $\alpha_{PT}$ . The maximum calibrated daily  $\alpha_{PT}$  is close to the  
545 theoretical value of 1.26 for all three sites. However its temporal variability is found to be  
546 significant even during the growing stage of wheat. A qualitative analysis of  $\alpha_{PT}$  variabilities  
547 in relation to soil moisture at 5 cm and 30 cm depth and to VWC indicates that  $\alpha_{PT}$  cannot be  
548 considered as a constant in the conditions of the experiments. Large deviations about the 1.26  
549 value are likely to occur during the agricultural season especially under dry, water deficit and  
550 advective conditions.

551 In terms of flux estimates, TSEB provides satisfying results for the flood site but not for the  
552 other two (controlled and reference drip) sites. The saturation of TSEB in the higher range of  
553 ET is due to the fixed maximum value for  $\alpha_{PT}$  (equal to 1.26). Moreover, the overestimation of  
554 LE by TSEB during senescence is associated with a very low sensitivity of simulated H to any  
555 surface/atmospheric conditions. Both limitations identified in the TSEB formalism seem to be  
556 partly solved by the TSEB-SM approach with a slope of the linear regression between  
557 simulated and observed LE/H much closer to 1 in all cases. Such an evapotranspiration model  
558 simultaneously constrained by LST,  $f_c$  and SM seems to respond robustly in terms of LE/H  
559 partitioning for wheat crops under the conditions of the experiments. However, the calibrated  
560 daily  $\alpha_{PT}$  needed to be i) smoothed to reduce random uncertainties and ii) normalized between  
561 its two extreme values since the 0 value was not necessarily reached at harvest. In the real  
562 application the use of NDVI as a green vegetation index would provide complementary  
563 information to constrain even more the drop in the retrieved “effective  $\alpha_{PT}$ ” during senescence.  
564 Further efforts should be made to investigate the variability of  $\alpha_{PT}$  at the daily and finer time  
565 scales and to relate its variations to variables other than biomass and soil water availability.  
566 Reciprocally, the retrieved  $\alpha_{PT}$  could serve as a basis for deriving a proxy for root zone soil  
567 moisture and crop water needs. Last but not least estimates of SM are needed at the crop field  
568 scale. Those data may be provided by satellite microwave data disaggregated at medium to  
569 high spatial resolution (Merlin et al., 2013; Molero et al., 2016). Especially, the L4DIS  
570 processor (Merlin et al., 2012; Molero et al., 2016) provides 1 km resolution SM data on a  
571 routine basis from 40 km resolution Soil Moisture and Ocean Salinity (SMOS) and 1 km  
572 resolution MODIS (Moderate resolution Imaging Spectroradiometer) data. Such a high-  
573 resolution SM product would be fully compatible with future implementations of TSEB-SM  
574 over large areas.

## 575 **Acknowledgments**

576 Initial set up and maintenance of the field instrumentation (R3 and Chichawa) are funded by  
577 the Joint International Laboratory TREMA <http://trema.ucam.ac.ma>. This study was partly  
578 supported by the European Commission Horizon 2020 Programme for Research and  
579 Innovation (H2020) in the context of the Marie Skłodowska-Curie Research and Innovation  
580 Staff Exchange (RISE) action (REC project. grant agreement no: 645642) and the French  
581 Agence Nationale de la Recherche (MIXMOD-E project. ANR-13-JS06-003-01). Additional  
582 funding was provided by the ANR-AMETHYST project (ANR-12-TMED-0006-01). The  
583 ARTS fellowship program from Institut de Recherche pour le Développement (IRD) is fully  
584 acknowledged.

## 585 **References**

586 Agam, N., Kustas, W. P., Anderson, M. C., Norman, J. M., Colaizzi, P. D., Howell, T. A., ...  
587 & Wilson, T. B. (2010). Application of the Priestley–Taylor approach in a two-source  
588 surface energy balance model. *Journal of Hydrometeorology*, 11(1), 185-198.

- 589 Ai, Z., & Yang, Y. (2016). Modification and Validation of Priestley–Taylor Model for  
590 Estimating Cotton Evapotranspiration under Plastic Mulch Condition. *Journal of*  
591 *Hydrometeorology*, 17(4), 1281-1293.
- 592 Albergel, C., Rüdiger, C., Pellarin, T., Calvet, J. C., Fritz, N., Froissard, F., ... & Martin, E.  
593 (2008). From near-surface to root-zone soil moisture using an exponential filter: an  
594 assessment of the method based on in-situ observations and model  
595 simulations. *Hydrology and Earth System Sciences Discussions*, 12, 1323-1337.
- 596 Allen, R. G., Pereira, L. S., Raes, D., & Smith, M. (1998). Crop evapotranspiration-Guidelines  
597 for computing crop water requirements-FAO Irrigation and drainage paper 56. *FAO*,  
598 *Rome*, 300(9), D05109.
- 599 Allen, R. G. (2000). Using the FAO-56 dual crop coefficient method over an irrigated region  
600 as part of an evapotranspiration intercomparison study. *Journal of Hydrology*, 229(1),  
601 27-41.
- 602 Allen, R. G., Pereira, L. S., Howell, T. A., & Jensen, M. E. (2011). Evapotranspiration  
603 information reporting: I. Factors governing measurement accuracy. *Agricultural*  
604 *Water Management*, 98(6), 899-920.
- 605 Anderson, M. C., Norman, J. M., Mecikalski, J. R., Otkin, J. A., & Kustas, W. P. (2007). A  
606 climatological study of evapotranspiration and moisture stress across the continental  
607 United States based on thermal remote sensing: 1. Model formulation. *Journal of*  
608 *Geophysical Research: Atmospheres*, 112(D10).
- 609 Bindlish, R., Kustas, W. P., French, A. N., Diak, G. R., & Mecikalski, J. R. (2001). Influence  
610 of near-surface soil moisture on regional scale heat fluxes: Model results using  
611 microwave remote sensing data from SGP97. *IEEE transactions on geoscience and*  
612 *remote sensing*, 39(8), 1719-1728.
- 613 Brutsaert, W., (1982). *Evaporation Into The Atmosphere*. Reidel, Dordrecht, 299 pp.
- 614 Chanzy, A., & Bruckler, L. (1993). Significance of soil surface moisture with respect to daily  
615 bare soil evaporation. *Water Resources Research*, 29(4), 1113-1125.
- 616 Chehbouni, A., Escadafal, R., Duchemin, B., Boulet, G., Simonneaux, V., Dedieu, G., ... &  
617 Sobrino, J. (2008). An integrated modelling and remote sensing approach for  
618 hydrological study in arid and semi-arid regions: The SUDMED  
619 Programme. *International Journal of Remote Sensing*, 29(17-18), 5161-5181.
- 620 Chirouze, J., Boulet, G., Jarlan, L., Fieuzal, R., Rodriguez, J.C., Ezzahar, J., Er-Raki, S.,  
621 Bigeard, G., Merlin, O., Garatuza-Payan, J., Watts, C., Chehbouni, G., 2014.  
622 Intercomparison of four remote-sensing-based energy balance methods to retrieve  
623 surface evapotranspiration and water stress of irrigated fields in semi-arid climate.  
624 *Hydrol. Earth Syst. Sci.* 18, 1165–1188.
- 625 Choudhury, B.J., Idso, S., & Reginato R. (1987). Analysis of an empirical model for soil heat  
626 flux under a growing wheat crop for estimating evaporation by an infrared-temperature  
627 based energy balance equation. *Agricultural and Forest Meteorology*, 39(4), 283–297.
- 628 Colaizzi, P. D., Evett, S. R., Howell, T. A., Gowda, P. H., O’Shaughnessy, S. A., Tolck, J. A.,  
629 Kustas, W. P., & Anderson, M. C.(2012). Two-source energy balance model:  
630 Rrefinements and lysimeter tests in the Southern High Plains. *Trans. ASABE*, 55(2),  
631 551-562.

- 632 Colaizzi, P. D., Agam, N., Tolk, J. A., Evett, S. R., Howell, T. A., Gowda, P. H., ... & Anderson,  
633 M. C. (2014). Two source energy balance model to calculate E, T, and ET: Comparison  
634 of Priestley-Taylor and Penman-Monteith formulations and two time scaling  
635 methods. *Trans. Asabe*, 57(2), 479-498.
- 636 Dai Yongjiu and Zeng Qingcun. 1997. A land surface model (IAP94) for climate studies part  
637 I: Formulation and validation in off-line experiments. *Advances in Atmospheric*  
638 *Sciences*, 14, 433-460.
- 639 Davies, J. A., & Allen, C. D. (1973). Equilibrium, potential and actual evaporation from  
640 cropped surfaces in southern Ontario. *Journal of Applied Meteorology*, 12(4), 649-657.
- 641 De Bruin, H. A. R. (1983). A model for the Priestley-Taylor parameter  $\alpha$ . *Journal of climate*  
642 *and applied meteorology*, 22(4), 572-578.
- 643 Diarra A., Jarlan L., Er-Raki S., Le Page M., Aouade G., Tavernier A., Boulet G, Ezzahar J.,  
644 Merlin O., & Khabba S. (2017). Performance of the two-source energy budget (TSEB)  
645 model for the monitoring of evapotranspiration over irrigated annual crops in North  
646 Africa, submitted to *Agriculture water management*.
- 647 Eichinger. W. E., Parlange. M. B., & Stricker. H. (1996). On the concept of equilibrium  
648 evaporation and the value of the priestley-taylor coefficient. *Water Resources*  
649 *Research*. 32(1). 161-164.
- 650 Er-Raki, S., Chehbouni, A., Guemouria, N., Duchemin, B., Ezzahar, J., Hadria, R. (2007).  
651 Combining FAO-56 model and ground-based remote sensing to estimate water  
652 consumptions of wheat crops in a semi-arid region. *Agricultural Water Management*,  
653 87, 41-54.
- 654 Er-Raki, S., Chehbouni, A., Khabba, S., Simonneaux, V., Jarlan, L., Ouldbba, A., Rodriguez,  
655 J.C., Allen, R. (2010). Assessment of reference evapotranspiration methods in semi-  
656 arid regions: Can weather forecast data be used as alternate of ground meteorological  
657 parameters? *Journal of Arid Environments*. 74, 1587-1596.
- 658 Eichinger, W. E., Parlange, M. B., & Stricker, H. (1996). On the concept of equilibrium  
659 evaporation and the value of the priestley-taylor coefficient. *Water Resources*  
660 *Research*, 32(1), 161-164.
- 661 Ershadi, A., McCabe, M. F., Evans, J. P., Chaney, N. W., & Wood, E. F. (2014). Multi-site  
662 evaluation of terrestrial evaporation models using FLUXNET data. *Agricultural and*  
663 *Forest Meteorology*, 187, 46-61.
- 664 Ezzahar, J., Chehbouni, A., Er-Raki, S., & Hanich, L. (2009). Combining a large aperture  
665 scintillometer and estimates of available energy to derive evapotranspiration over  
666 several agricultural fields in a semi-arid region, *Plant Biosystems*, 143(1), 209-221
- 667 Federer, C. A., Vörösmarty, C., & Fekete, B. (2003). Sensitivity of annual evaporation to soil  
668 and root properties in two models of contrasting complexity. *Journal of*  
669 *Hydrometeorology*, 4(6), 1276-1290.
- 670 Fisher, J. B., Tu, K. P., & Baldocchi, D. D. (2008). Global estimates of the land-atmosphere  
671 water flux based on monthly AVHRR and ISLSCP-II data, validated at 16 FLUXNET  
672 sites. *Remote Sensing of Environment*, 112(3), 901-919.
- 673 French, A. N., Hunsaker, D. J., & Thorp, K. R. (2015). Remote sensing of evapotranspiration  
674 over cotton using the TSEB and METRIC energy balance models. *Remote Sens.*  
675 *Environ.*, 158, 281-294.

- 676 Gentine, P., Entekhabi, D., Chehbouni, A., Boulet, G., and Duchemin, B. (2007): Analysis of  
677 evaporative fraction diurnal behaviour. *Agric. For. Meteorol.*, 143, 13–29.
- 678 Gharsallah O., Facchi A., Gandolf C. (2013). Comparison of six evapotranspiration models  
679 for a surface irrigated maize agro-ecosystem in Northern Italy. *Agricultural Water*  
680 *Management*, 130, 119–130
- 681 Gokmen, M., Vekerdy, Z., Verhoef, A., Verhoef, W., Batelaan, O., & Van der Tol, C. (2012).  
682 Integration of soil moisture in SEBS for improving evapotranspiration estimation under  
683 water stress conditions. *Remote Sensing of Environment*, 121, 261-274.
- 684 Hain, C. R., Mecikalski, J. R., & Anderson, M. C. (2009). Retrieval of an available water-based  
685 soil moisture proxy from thermal infrared remote sensing. Part I: Methodology and  
686 validation. *Journal of Hydrometeorology*, 10(3), 665-683.
- 687 Jarlan, L., Khabba, S., Er-Raki, S., Le Page, M., Hanich, L., Fakir, Y., ... & Kharrou, M. H.  
688 (2015). Remote sensing of water resources in semi-arid Mediterranean areas: The joint  
689 international laboratory TREMA. *International Journal of Remote Sensing*, 36(19-20),  
690 4879-4917.
- 691 Jiang, L., & Islam, S. (2001). Estimation of surface evaporation map over southern Great Plains  
692 using remote sensing data. *Water resources research*, 37(2), 329-340.
- 693 Jin, Y., Randerson, J. T., & Goulden, M. L. (2011). Continental-scale net radiation and  
694 evapotranspiration estimated using MODIS satellite observations. *Remote Sensing of*  
695 *Environment*, 115(9), 2302-2319.
- 696 Jung, M., Reichstein, M., Ciais, P., Seneviratne, S. I., Sheffield, J., Goulden, M. L., ... &  
697 Dolman, A. J. (2010). Recent decline in the global land evapotranspiration trend due to  
698 limited moisture supply. *Nature*, 467(7318), 951-954.
- 699 Jury, W. A., & Tanner, C. B. (1975). Advection modification of the Priestley and Taylor  
700 evapotranspiration formula. *Agronomy Journal*, 67(6), 840-842.
- 701 Kalma J.D., McVicar T.R., and McCabe M.F. (2008). Estimating Land Surface Evaporation:  
702 A Review of Methods Using Remotely Sensed Surface Temperature Data. *Surv*  
703 *Geophys*, 29, 421–469.
- 704 Khabba, S., Duchemin B., Hadria, R., Ezzahar J., Chehbouni A., Lahrouni A., Hanich L.(2009).  
705 Evaluation of digital hemispherical photography and plant canopy analyser for  
706 measuring Vegetation area index of orange orchards. *Journal of Agronomy*, 8(2), 67-  
707 72.
- 708 Kustas, W.P., & Norman, J.M. (1997). A two-source approach for estimating turbulent fluxes  
709 using multiple angle thermal infrared observations. *Water resources research*,  
710 33(6),1495–1508.
- 711 Kustas, W. P., Zhan, X., & Schmugge, T. J. (1998). Combining optical and microwave remote  
712 sensing for mapping energy fluxes in a semiarid watershed. *Remote Sensing of*  
713 *Environment*, 64(2), 116-131.
- 714 Kustas, W. P., Zhan, X., & Jackson, T. J. (1999). Mapping surface energy flux partitioning at  
715 large scales with optical and microwave remote sensing data from Washita'92. *Water*  
716 *resources research*, 35(1), 265-277.

- 717 Kustas, W. P., & Norman, J. M. (1999). Evaluation of soil and vegetation heat flux predictions  
718 using a simple two-source model with radiometric temperatures for partial canopy  
719 cover. *Agricultural and Forest Meteorology*, 94(1), 13-29
- 720 Kustas, W.P., Prueger, J.H., Hatfield, J.L., Ramalingam, H., & Hipps, L.E. (2000).  
721 Variability in soil heat flux from a mesquite dune site. *Agricultural and Forest*  
722 *Meteorology*,103(1), 249-264.
- 723 Kustas, W. P., Bindlish, R., French, A. N., & Schmugge, T. J. (2003). Comparison of energy  
724 balance modeling schemes using microwave-derived soil moisture and radiometric  
725 surface temperature. *Water resources research*, 39(2).
- 726 Lhomme, J. P., Boudhina, N., Masmoudi, M. M., and Chehbouni, A.(2015). Estimation of  
727 crop water requirements: extending the one-step approach to dual crop coefficients.  
728 *Hydrol. Earth Syst. Sci.* 19, 3287-3299.
- 729 Li, F., Kustas, W. P., Prueger, J. H., Neale, C. M., & Jackson, T. J. (2005). Utility of remote  
730 sensing-based two-source energy balance model under low-and high-vegetation cover  
731 conditions. *Journal of Hydrometeorology*, 6(6), 878-891.
- 732 Li, F., Kustas, W. P., Anderson, M. C., Jackson, T. J., Bindlish, R., & Prueger, J. H. (2006).  
733 Comparing the utility of microwave and thermal remote-sensing constraints in two-  
734 source energy balance modeling over an agricultural landscape. *Remote sensing of*  
735 *environment*, 101(3), 315-328.
- 736 Li, F., Crow, W. T., & Kustas, W. P. (2010). Towards the estimation root-zone soil moisture  
737 via the simultaneous assimilation of thermal and microwave soil moisture  
738 retrievals. *Advances in Water Resources*, 33(2), 201-214.
- 739 Li, Y., Zhou, J., Wang, H., Li, D., Jin, R., Zhou, Y., & Zhou, Q. (2015). Integrating soil  
740 moisture retrieved from L-band microwave radiation into an energy balance model to  
741 improve evapotranspiration estimation on the irrigated oases of arid regions in  
742 northwest China. *Agricultural and Forest Meteorology*, 214, 306-318.
- 743 Long, D., & Singh, V. P. (2012). A two-source trapezoid model for evapotranspiration (TTME)  
744 from satellite imagery. *Remote Sensing of Environment*, 121, 370-388.
- 745 Martínez Pérez, J. Á., García-Galiano, S. G., Martín-Gorriz, B., & Baille, A. (2017). Satellite-  
746 Based Method for Estimating the Spatial Distribution of Crop Evapotranspiration:  
747 Sensitivity to the Priestley-Taylor Coefficient. *Remote Sensing*, 9(6), 611.
- 748 McAneney, K. J., & Itier, B. (1996). Operational limits to the Priestley-Taylor  
749 formula. *Irrigation Science*, 17(1), 37-43.
- 750 Merlin, O., Al Bitar, A., Rivalland, V., Béziat, P., Ceschia, E., & Dedieu, G. (2011). An  
751 analytical model of evaporation efficiency for unsaturated soil surfaces with an  
752 arbitrary thickness. *Journal of Applied Meteorology and Climatology*, 50(2), 457-471.
- 753 Merlin, O., Rudiger, C., Al Bitar, A., Richaume, P., Walker, J. P., & Kerr, Y. H. (2012).  
754 Disaggregation of SMOS soil moisture in Southeastern Australia. *IEEE Transactions*  
755 *on Geoscience and Remote Sensing*, 50(5), 1556-1571.
- 756
- 757

- 758 Merlin, O., Escorihuela, M. J., Mayoral, M. A., Hagolle, O., Al Bitar, A., & Kerr, Y. (2013).  
 759 Self-calibrated evaporation-based disaggregation of SMOS soil moisture: An  
 760 evaluation study at 3km and 100m resolution in Catalunya, Spain. *Remote sensing of*  
 761 *environment*, 130, 25-38.
- 762 Merlin, O., Chirouze, J., Olivoso, A., Jarlan, L., Chehbouni, G., & Boulet, G. (2014). An image-  
 763 based four-source surface energy balance model to estimate crop evapotranspiration  
 764 from solar reflectance/thermal emission data (SEB-4S). *Agricultural and Forest*  
 765 *Meteorology*, 184, 188-203.
- 766 Merlin, O., Stefan, V. G., Amazirh, A., Chanzy, A., Ceschia, E., Er-Raki, S., ... & Beringer, J.  
 767 (2016). Modeling soil evaporation efficiency in a range of soil and atmospheric  
 768 conditions using a meta-analysis approach. *Water Resources Research*, 52(5), 3663-  
 769 3684.
- 770 Merlin, O., Olivera-Guerra, L., Aït Hssaine, B., Amazirh, A., Rafi, Z., Ezzahar, J., Gentine, P.,  
 771 Khabba, S., Gascoin, S., Er-Raki, S., A phenomenological model of soil evaporative  
 772 efficiency using readily available data, submitted to *Agricultural and Forest*  
 773 *Meteorology*.
- 774 Molero, B., Merlin, O., Malbêteau, Y., Al Bitar, A., Cabot, F., Stefan, V., ... & Jackson, T. J.  
 775 (2016). SMOS disaggregated soil moisture product at 1km resolution: Processor  
 776 overview and first validation results. *Remote Sensing of Environment*, 180, 361-376.
- 777 Monteith, J. L. (1965, July). Evaporation and environment. In *Symp. Soc. Exp. Biol* , 19(4),  
 778 205-23.
- 779 Moran, M. S., Clarke, T. R., Inoue, Y., & Vidal, A. (1994). Estimating crop water deficit using  
 780 the relation between surface-air temperature and spectral vegetation index. *Remote*  
 781 *sensing of environment*, 49(3), 246-263.
- 782 Mukammal, E. I., & Neumann, H. H. (1977). Application of the Priestley-Taylor evaporation  
 783 model to assess the influence of soil moisture on the evaporation from a large weighing  
 784 lysimeter and class A pan. *Boundary-Layer Meteorology*, 12(2), 243-256.
- 785 Norman, J. M., Kustas, W. P., & Humes, K. S. (1995). Two source approach for estimating  
 786 soil and vegetation energy fluxes in observations of directional radiometric surface  
 787 temperature. *Agricultural and Forest Meteorology*, 77(3), 263-293.
- 788 Oleson, K. W., Niu, G. Y., Yang, Z. L., Lawrence, D. M., Thornton, P. E., Lawrence, P. J.,  
 789 Stockli, R., Dickinson, R. E., Bonan, G. B., and Levis, S. (2008). Improvements to the  
 790 Community Land Model and their impact on the hydrological cycle, *J. Geophys. Res.*,  
 791 113, G01021, doi:10.1029/2007JG000563.
- 792 Passerat de Silans, A., 1986. Transferts de masse et de chaleur dans un sol stratifié soumis une  
 793 excitation atmosphérique naturelle. Comparaison son modèle expérience. PhD Thesis,  
 794 Institut National Polytechnique de Grenoble, France.
- 795 Pereira, A. R., & Nova, N. A. V. (1992). Analysis of the Priestley-Taylor  
 796 parameter. *Agricultural and Forest Meteorology*, 61(1-2), 1-9.
- 797 Pereira, A. R. (2004). The Priestley–Taylor parameter and the decoupling factor for estimating  
 798 reference evapotranspiration. *Agricultural and Forest Meteorology*, 125(3), 305-313.

- 799 Price, J. C. (1990). Using spatial context in satellite data to infer regional scale  
800 evapotranspiration. *IEEE transactions on Geoscience and Remote Sensing*, 28(5), 940-  
801 948.
- 802 Priestley, C. H. B., & Taylor, R. J. (1972). On the assessment of surface heat flux and  
803 evaporation using large-scale parameters. *Monthly weather review*, 100(2), 81-92.
- 804 Roerink, G. J., Su, Z., & Menenti, M. (2000). S-SEBI: A simple remote sensing algorithm to  
805 estimate the surface energy balance. *Physics and Chemistry of the Earth. Part B:*  
806 *Hydrology, Oceans and Atmosphere*, 25(2), 147–157.
- 807 Sauer, T. J., Norman, J. M., Tanner, C. B., & Wilson, T. B. (1995). Measurement of heat and  
808 vapor transfer at the soil surface beneath a maize canopy using source plates.  
809 *Agricultural and Forest Meteorology*, 75, 161-189.
- 810 Sellers, P. J., Heiser, M. D., & Hall, F. G. (1992). Relations between surface conductance and  
811 spectral vegetation indices at intermediate (100 m<sup>2</sup> to 15 km<sup>2</sup>) length scales. *Journal*  
812 *of Geophysical Research*, 97(D17), 19-033.
- 813 Song, L., Kustas, W. P., Liu, S., Colaizzi, P. D., Nieto, H., Xu, Z., ... & Tolck, J. A. (2016).  
814 Applications of a thermal-based two-source energy balance model using Priestley-  
815 Taylor approach for surface temperature partitioning under advective  
816 conditions. *Journal of Hydrology*, 540, 574-587.
- 817 Su, Z. (2002). The Surface Energy Balance System (SEBS) for estimation of turbulent heat  
818 fluxes. *Hydrology and Earth System Sciences*, 6(1), 85-100.
- 819 Sun, J., Salvucci, G. D., & Entekhabi, D. (2012). Estimates of evapotranspiration from MODIS  
820 and AMSR-E land surface temperature and moisture over the Southern Great  
821 Plains. *Remote sensing of environment*, 127, 44-59.
- 822 Timmermans, W.J., Kustas, W.P., Anderson, M.C., French, A.N. (2007). An intercomparison  
823 of the surface energy balance algorithm for land (SEBAL) and the two-source energy  
824 balance (TSEB) modeling schemes. *Remote Sensing of Environment*. 108, 369–384.
- 825 Twine, T.E., Kustas, W.P., Norman, J.M., Cook, D.R., & Houser, P.R. (2000). Correcting eddy-  
826 covariance flux underestimation over a grassland. *Agricultural and Forest*  
827 *Meteorology*, 103(3), 279-300.
- 828 Van de Griend, A. A., and Owe M. (1994). Bare soil surface resistance to evaporation by vapor  
829 diffusion under semiarid conditions, *Water Resour. Res.*, 30(2), 181–188.
- 830 Van Dijk, A., Moene A. F., & de Bruin H. A. R. (2004). The principles of surface flux  
831 physics: Theory. *Practice and Description of the ECPACK Library*, 99-100.
- 832 Wang, K., Li, Z., & Cribb, M. (2006). Estimation of evaporative fraction from a combination  
833 of day and night land surface temperatures and NDVI: A new method to determine the  
834 Priestley–Taylor parameter. *Remote Sensing of Environment*, 102(3), 293-305.
- 835 Yao, Y., Liang, S., Li, X., Chen, J., Wang, K., Jia, K., ... & Grünwald, T. (2015). A satellite-  
836 based hybrid algorithm to determine the Priestley–Taylor parameter for global  
837 terrestrial latent heat flux estimation across multiple biomes. *Remote Sensing of*  
838 *Environment*, 165, 216-233.



839 Yao, Y., Liang, S., Yu, J., Zhao, S., Lin, Y., Jia, K., ... & Wang, X. (2017). Differences in  
840 estimating terrestrial water flux from three satellite-based Priestley-Taylor  
841 algorithms. *International Journal of Applied Earth Observation and*  
842 *Geoinformation*, 56, 1-12.  
843  
844  
845  
846